

Scatter Correction for Dual-source Cone-beam CT Using the Pre-patient Grid

by

Yingxuan Chen

Graduate Program in Medical Physics
Duke University

Date: _____

Approved:

Lei Ren, Supervisor

Fang-Fang Yin, Chair

James T. Dobbins III

Thesis submitted in partial fulfillment of
the requirements for the degree of
Master of Science in the Graduate Program in
Medical Physics in the Graduate School
of Duke University

2014

ABSTRACT

Scatter Correction for Dual-source Cone-beam CT Using the Pre-patient Grid

by

Yingxuan Chen

Graduate Program in Medical Physics
Duke University

Date: _____

Approved:

Lei Ren, Supervisor

Fang-Fang Yin, Chair

James T. Dobbins III

An abstract of a thesis submitted in partial fulfillment of
the requirements for the degree of
Master of Science in the Graduate Program in
Medical Physics in the Graduate School
of Duke University

2014

Copyright by
Yingxuan Chen
2014

Abstract

Purpose: A variety of cone beam CT (CBCT) systems has been used in the clinic for image guidance in interventional radiology and radiation therapy. Compared with conventional single-source CBCT, dual-source CBCT has the potential for dual-energy imaging and faster scanning. However, it adds additional cross-scatter when compared to a single-source CBCT system, which degrades the image quality. Previously, we developed a synchronized moving grid (SMOG) system to reduce and correct scatter for a single-source CBCT system. The purpose of this work is to implement the SMOG system on a prototype dual-source CBCT system and to investigate its efficacy in scatter reduction and correction under various imaging acquisition settings.

Methods: A 1-D grid was attached to each x-ray source during dual-source CBCT imaging to acquire partially blocked projections. As the grid partially blocked the x-ray primary beams and divided it into multiple quasi-fan beams during the scan, it produced a physical scatter reduction effect in the projections. Phantom data were acquired in the unblocked area, while scatter signal was measured from the blocked area in projections. The scatter distribution was estimated from the measured scatter signals using a cubic spline interpolation for post-scan scatter correction. Complimentary partially blocked projections were acquired at each scan angle by positioning the grid at different locations, and were merged to obtain full projections for reconstruction. In this

study, three sets of CBCT images were reconstructed from projections acquired: (a) without grid, (b) with grid but without scatter correction, and (c) with grid and with scatter correction to evaluate the effects of scatter reduction and scatter correction on artifact reduction and improvements of contrast-to-noise ratio index (CNR') and CT number accuracy. The efficacy of the scatter reduction and correction method was evaluated for CATphan phantoms of different diameters (15cm, 20cm, and 30cm), different grids (grid blocking ratios of 1:1 and 2:1), different acquisition modes (simultaneous: two tubes firing at the same time, interleaved: tube alternatively firing and sequential: only one tube firing in one rotation) and different reconstruction algorithms (iterative reconstruction method vs Feldkamp, Davis, and Kress (FDK) back projection method).

Results: The simultaneous scanning mode had the most severe scatter artifacts and the most degraded CNR' when compared to either the interleaved mode or the sequential mode. This is due to the cross-scatter between the two x-ray sources in the simultaneous mode. Scatter artifacts were substantially reduced by scatter reduction and correction. CNR's of the different inserts in the CATphan were enhanced on average by 24%, 13%, and 33% for phantom sizes of 15cm, 20cm, and 30cm, respectively, with only scatter reduction and a 1:1 grid. Correspondingly, CNR's were enhanced by 34%, 18%, and 11%, respectively, with both scatter reduction and correction. However, CNR' may decrease with scatter correction alone for the larger phantom and low contrast ROIs,

because of an increase in noise after scatter correction. In addition, the reconstructed HU numbers were linearly correlated to nominal HU numbers. A higher grid blocking ratio, i.e. with a greater blocked area, resulted in better scatter artifact removal and CNR' improvement at the cost of complexity and increased number of exposures. Iterative reconstruction with total variation regularization resulted in better noise reduction and enhanced CNR', in comparison to the FDK method.

Conclusion: Our method with a pre-patient grid can effectively reduce the scatter artifacts, enhance CNR', and modestly improve the CT number linearity for the dual-source CBCT system. The settings such as grid blocking ratio and acquisition mode can be optimized based on the patient-specific condition to further improve image quality.

Contents

Abstract	iv
List of Tables	x
List of Figures	xii
Acknowledgements	xv
1. Introduction and Background	1
1.1 Computed Tomography	1
1.1.1 Development of Computed Tomography	1
1.1.2 Flat Panel Based Cone Beam CT (CBCT) for Image Guide Radiation Therapy	2
1.1.3 Dual-source CBCT	3
1.2 Scatter Effects on CBCT	3
1.3 Scatter Suppression for CBCT.....	5
1.3.1 Scatter Reduction Methods	5
1.3.2 Scatter Correction Methods.....	6
1.3.3 Combining Scatter Reduction and Correction in a Synchronized Moving Grid (SMOG) System	8
1.4 Research Aim	8
2. Materials and Methods.....	10
2.1 Experiment Equipment.....	10
2.1.1 Dual-source CBCT System	10
2.1.2 Pre-patient Grid	11
2.1.3 Phantom.....	12

2.2 Experiment Setup	14
2.2.1 Basic Setup.....	14
2.2.2 Acquisition Mode.....	16
2.2.3 Data Description.....	17
2.3 Scatter Correction Algorithm.....	17
2.4 Reconstruction Algorithm.....	23
2.5 Image Quality Assessment.....	23
2.5.1 Qualitative Assessment on Artifact	24
2.5.2 Contrast-to-noise Ratio Index (CNR')	24
2.5.3 HU Number Linearity	26
2.5.4 Uniformity	26
3. Results.....	28
3.1 Scatter Artifact, Scatter Reduction and Correction.....	28
3.2 Contrast-to-noise Ratio Index (CNR')	33
3.3 HU Number Linearity	38
3.4 Uniformity	40
4. Discussion	41
4.1 Scatter Reduction and Scatter Correction with Various Experimental Settings....	41
4.1.1 Cross Scatter.....	44
4.1.2 Scatter vs. Phantom Size.....	44
4.1.3 Grid Effect.....	45
4.2 Reconstruction Algorithm.....	46

4.3 Limitation of Scatter Correction with Pre-patient Grid	47
4.3.1 Noise.....	47
4.3.2 Image Lag	48
4.3.3 Artifact of Grid Misalignment	48
5. Conclusion	52
References	53

List of Tables

Table 2-1. Name, consistence and the function of each module in Catphan 504.	13
Table 2-2. Experimental conditions investigated in the study.	17
Table 3-1. Comparison between CNR' of 8 inserts in three image sets: original CBCT, CBCT reconstructed with scatter reduction only and CBCT reconstructed with scatter reduction and correction. Phantom of 20cm diameter, 1:1 grid and simultaneous mode were used in the scan.	34
Table 3-2. Comparison between CNR' in images acquired by the simultaneous and sequential scanning modes. Phantom of 20cm diameter and 1:1 grid was used in the scan.	35
Table 3-3. Comparison between CNR' acquired by simultaneous, interleaved and sequential modes. Phantom of 20cm diameter and 2:1 grid was used in the scan.....	35
Table 3-4. Comparison between CNR' in CBCT images acquired by various phantom sizes.	36
Table 3-5. Comparison between CNR' in CBCT images acquired with different grid blocking ratios (1:1 and 2:1 grids).....	37
Table 3-6. Comparison between CNR' in CBCT images reconstructed by the FDK and iterative method.	37
Table 3-7. Regression coefficients R^2 between reconstructed and nominal HU values for various experimental settings.	38
Table 3-8. HU accuracy in reconstructed CBCT images of the 20cm-diameter phantom acquired with the 1:1 grid and the simultaneous scanning mode.	39
Table 3-9. Uniformity index of three image sets: original CBCT, CBCT reconstructed with scatter reduction only and CBCT reconstructed with scatter reduction and correction. The phantom of 20 cm diameter, 1:1 grid and simultaneous mode were used in this scan.....	40
Table 4-1. Comparison of the improvement of CNR' for various phantom sizes.	45

Table 4-2. Comparison of the improvement of CNR' enhancement for different grid blocking ratios.	46
---	----

List of Figures

Figure 2-1. The dual-source CBCT system with the CATphan phantom.	11
Figure 2-2. Three views of the (a) 1:1 grid and (b) 2:1 grid.	12
Figure 2-3. Picture of the (a) 1:1 grid and (b) 2:1 grid.	12
Figure 2-4. Picture of the phantom from the Catphan® 504 Manual.	13
Figure 2-5. Picture of the bowtie for the full fan scan. (a): Bowtie filter. (b): Bowtie attached on the tube.....	14
Figure 2-6. Schematic diagram of the SMOG system in the dual-source CBCT system. Both the forward scatter and the cross scatter will reach the detector. Grid is put between the patient and the tube.....	15
Figure 2-7. Diagram of the x-ray source. (a) Left sagittal view of the source. (b) Image of the bowtie filter and the grid attached to the source.	16
Figure 2-8. An example to illustrate the scatter correction procedure using 1:1 grid.	19
Figure 2-9. An example illustrating the scatter estimation and correction process in an empty scan. The blue solid line is original 1 D profile in the longitudinal direction in an empty scan projection. The star dots are the measured scatter in the blocked areas. The black line is the interpolated scatter distribution. The red solid line is final profile after scatter correction by subtracting the black line from the blue line.	20
Figure 2-10. An example illustrating the scatter estimation and correction process in a phantom scan. The blue solid line is original 1 D profile in the longitudinal direction in a phantom scan projection at a specific angle. The star dots are the measured scatter in the blocked area. The black line is interpolated scatter distribution. The red solid line is final profile after scatter correction by subtracting the black line from the blue line.	21
Figure 2-11. Profiles extracted from complementary projections after empty scan normalization and negative logarithm transformation. (a) The red and blue solid lines were from two complementary projections acquired with the grid shifted by one grid inter-space. (b) Profile of the merged projection.	22

Figure 2-12. Axial view of the CTP404 module with eight different inserts reconstructed by the FDK method. The red circles are the ROIs inside the inserts while the yellow ones are the ROIs surrounding the inserts. 25

Figure 2-13. Nominal HU values of the eight inserts in the CTP404 module. 26

Figure 2-14. Axial view of the CTP486 uniformity module of the CATphan. Five ROIs were defined (one is in the center and the other four are at the edge) to calculate the uniformity of the image. 27

Figure 3-1. Reconstructed images of a CATphan of 20cm diameter using 1) simultaneous and 2) sequential acquisition mode. 1:1 grid was applied for scatter reduction and scatter correction. From left to right column: (a) without grid, (b) scatter reduction only and (c) scatter reduction and correction. Window width of 1000HU and window level of -200HU were used for all images..... 28

Figure 3-2. Reconstructed images of a CATphan of 20cm diameter using 1) simultaneous, 2) interleaved and 3) sequential acquisition mode. 2:1 grid was applied for scatter reduction and scatter correction. From left to right column: (a) without grid, (b) scatter reduction only and (c) scatter reduction and correction. Window width of 1000HU and window level of -200HU were used for all images. 29

Figure 3-3. Reconstructed images of a CATphan of 15, 20 and 30cm diameters (from 1st to 3rd row) acquired by simultaneous mode (dual-source). 1:1 grid was applied for scatter reduction and scatter correction. From left to right column: (a) without grid, (b) scatter reduction only and (c) scatter reduction and correction. Display for 1st and 2nd: window width of 1000HU and window level of -200HU were used. Display for 3rd: window width of 2200HU and window level of 100HU were used. 30

Figure 3-4. Reconstructed images of a CATphan of 20 cm diameter acquired by simultaneous mode (dual-source). 1:1(1st row) and 2:1grid (2nd row) was applied for scatter reduction and scatter correction. From left to right column: (a) without grid, (b) scatter reduction only and (c) scatter reduction and correction. Window width of 1000HU and window level of -200HU were used for all images..... 31

Figure 3-5. Reconstructed images of a CATphan of 20cm diameter acquired by simultaneous mode (dual-source). 1:1 was applied for scatter reduction and scatter correction. Images were reconstructed from the FDK method (1st row) and iterative method (2nd row). From left to right column: (a) without grid, (b) scatter reduction only

and (c) scatter reduction and correction. Window width of 1000HU and window level of -200HU were used for all images.....	32
Figure 3-6. Plot of the reconstructed HU value for each ROI vs. nominal HU values are shown for the 20cm-diameter phantom for different scatter reduction and correction techniques.	39
Figure 3-7. Reconstructed images of a CATphan of 20cm diameter (CTP 486: uniformity module) acquired by simultaneous mode (dual-source). 1:1 grid was applied for scatter reduction and scatter correction. From left to right: (a) without grid, (b) scatter reduction only and (c) scatter reduction and correction. Window width of 250HU and window level of 25HU were used for three images.	40
Figure 4-1. An example of image Lag. (a): exposure image acquired in an empty scan (pixel value min: 0, max: 14545). (b): image acquired by the same detector when the corresponding tube was not firing (pixel value min: 0, max: 283).....	48
Figure 4-2. An example of grid misalignment. (a). One merged projection for a CATphan of 20cm diameter acquired with a simultaneous mode using 1:1 grid. The arrows point out gaps caused by the misalignment between the grid shifts. (b). a sagittal slice of the reconstructed CBCT image. The noise region as pointed by arrows is caused by the gap in the projections in (a).	49
Figure 4-3. Reconstructed axial images of a CATphan of 20cm diameter scanned by the simultaneous acquisition mode. 1:1 grid was applied for scatter reduction and scatter correction. (a) without grid and (b) scatter reduction and scatter correction. Image is displayed with a window width of 1000HU and a window level of -200HU. As the arrows shown, streak artifacts caused by grid misalignment are shown as the noise region in the reconstructed image.	49
Figure 4-4. CNR' of 8 inserts in different reconstructed axial slices without grid using 20 cm CATphan acquired by simultaneous mode.	50
Figure 4-5. CNR' of 8 inserts in different reconstructed axial slices after scatter correction with 1:1 grid using 20 cm CATphan acquired by simultaneous mode.....	50

Acknowledgements

I would like to show my gratitude to my advisor, Dr. Lei Ren, for his generous guidance and encouragement in all steps of this project. I would also like to thank Dr. William Giles for his support on the experiment complement on the dual-source CBCT system. In addition, I want to thank You Zhang for his precious advice and help on CBCT reconstruction for this project. I am grateful to my committee members, Dr. Fang-Fang Yin and Dr. James Dobbins, for being on my thesis committee and for providing valuable suggestions to this project. Moreover, I also want to thank Anna Rodrigues and Titania Juang for proof reading and precious comments on the thesis writing. Finally, thanks to all the staff at Duke Radiation Oncology Department and the students in Medical Physics program who had lent a hand to this project.

1. Introduction and Background

1.1 Computed Tomography

Computed Tomography (CT), which is defined as the imaging modality that uses projections from several angles to produce 3D images, has been developed for over 40 years. In 1972, the first head CT scanner was introduced to view the structure in the human body [1]. Since then, CT technology has been widely used for diagnostic and image guidance purposes.

1.1.1 Development of Computed Tomography

To date, seven generations of CT have been developed. The first generation of CT scanner used pencil beam systems with single x-ray detector with the distance between x-ray tube and detectors kept constant. Data acquisition was achieved by translating the source and detectors in one direction to get one projection and then rotating them to get projections from multiple scan angles. The time for one slice scan, typically 270 seconds, was fairly long compared to the later generations of CT. The first generation CT was the best in terms of scatter reduction because of its use of pencil beams for scanning. The first generation was subsequently replaced by the second generation CT which increased the x-ray source beam angle and the size of the detector by 30 times to acquire the data more efficiently. However, this second generation CT with fan beam geometry still required translation of the source and the detector for data acquisition at each scan angle. The third generation CT was designed to remove the translation by using a wide fan

beam, which allows acquiring data only by rotating the tube and detectors synchronously. Instead of a row of detectors, the fourth generation CT used a stationary 360 degree ring of detectors and rotating x-ray tube. The fifth generation CT used the electron beam steering with stationary x-ray tube and ring detectors to achieve fast scanning. The sixth generation CT is helical CT which became possible through slip-ring gantry technology. Unlike the previous fan beam CT in which the acquisition needs to be stopped after each slice acquisition, helical CT allows continuous acquisition while the table is moving to image a larger volume, which substantially improves the scanning speed. Later on, multiple detector arrays in the axial dimension (seventh generation CT) were introduced in helical CT to further improve the scanning efficiency [1]. Helical and multiple array CT have been widely used in radiology and radiation oncology with the advantage of fast scanning (whole body scan in less than 1 minute). In recent years, one of the main trends of CT development has been to increase the x-ray beam angle and detectors size to acquire data more efficiently with a faster speed. Although multi-array helical CT are quick acquire and can generate high quality CT images, its application for image guidance in radiation therapy treatment is limited due to its large size and high cost.

1.1.2 Flat Panel Based Cone Beam CT (CBCT) for Image Guide Radiation Therapy

With the development of digital flat panel detectors, the on-board Cone Beam CT (CBCT) system has been introduced for on-board target localization in Image-Guided

Radiation Therapy (IGRT). In the on-board CBCT system, an x-ray source and on-board imager are attached to the linear accelerator (Linac) gantry, which can acquire cone-beam x-ray projections over a 360 degree gantry rotation to reconstruct patient volumetric images. CBCT has become a powerful tool for volumetric imaging verification in radiotherapy to improve the target localization accuracy. However, as the field size in CBCT is much larger than in helical CT, scatter effects are much more severe in CBCT causing scatter artifacts and degradation of image quality.

1.1.3 Dual-source CBCT

Dual-source CBCT, with dual sources and dual flat panel detectors, is superior to conventional CBCT and has several advanced applications in both radiology and radiation therapy. For example, dual-energy imaging can be approached without the use of the fast kV switching [2]. In addition, this design benefits 4D CT imaging because the scan time is reduced efficiently by the dual-source system. However, scatter effects are even more severe in a dual-source CBCT system than in a single-source CBCT because of increased cross-scatter radiation.

1.2 Scatter Effects on CBCT

In the diagnostic x-ray energy range of about 80-120 kVp, the dominant interaction between x-ray and the object is Compton scatter. During Compton interaction, the photon lose some of its energy to a loosely bound electron and changes its direction. In CT reconstruction, the attenuation coefficient of the material is calculated

based on Beer's law which accounts for the attenuation of the primary beam without scatter. In practice, the photons scattered by the object may be detected by the detector and increase the measured intensity of the x-ray. The integration of attenuation coefficients of the materials along a ray will be erroneously decreased due to the enhanced signal by scatter, which causes cupping and streak artifacts in the reconstructed images [3].

The x-ray scatter effect on CBCT image quality has been investigated in both simulation and experimental studies. The scatter effect is usually quantified by the scatter to primary ratio (SPR), which is usually greater than 100%. Several studies demonstrated that the scatter in CBCT results in scatter artifacts, inaccuracy in CT number and degradation of image contrast. For example, Jeffrey H. Siewerdsen [4] et al studied the relationship between image quality and SPR, and reported that both the noise and contrast were reduced as SPR was increased as the cone angle increased. Their results showed that CNR fell by a factor of 2 when SPR was about 120%. Yiannis Kyriakou [3] showed that the SPR is highly positively correlated to object size and x-ray imaging field size based on Monte Carlo simulation.

Overall, scatter has significant effects on CBCT, and need to be minimized in order to achieve high quality images for target localization.

1.3 Scatter Suppression for CBCT

As discussed in the previous section, radiation scatter plays a significant role in the degradation of the CBCT image quality by degrading image contrast and causing artifacts and inaccurate HU numbers. Many studies are being conducted to reduce the scatter and improve the image quality. In general, scatter suppression methods can be classified into two main groups: scatter reduction and scatter correction.

1.3.1 Scatter Reduction Methods

Scatter reduction methods include using collimation, a bow-tie filter, an anti-scatter grid or air gap to physically reduce the scatter detected by the imager. Scatter reduction using collimation, such as slot-scan, physically reduce the x-ray beam size to reduce the scatter [5]. An air gap and an anti-scatter grid are most commonly used in the clinic to reduce the scatter in x-ray radiography, mammography, and CT. The performance of the air gap and anti-scatter grid were evaluated by Neitzel [6], Sorenson et al [7] and Wiegert et al [8]. Increasing object-to-detector distance (air gap) reduces the SPR because fewer scatter photons will be detected by the detector. However, increasing object-to-detector distance will reduce the field of view of the reconstructed CBCT images. Therefore, the on-board CBCT system has a fixed isocenter-to-detector distance of 50cm to balance between scatter and image field of view. The benefit of an air gap or an anti-scatter grid is inherently limited because they can only reduce the scatter

radiation to a certain degree and cannot remove the scatter completely. Thus, additional methods are still needed for reducing the scatter effects in a CBCT system.

1.3.2 Scatter Correction Methods

Due to the limitation of the hardware scatter reduction methods, many researchers focused on reducing the scatter effects by performing post-scan scatter correction. Unlike scatter reduction methods, scatter correction methods can potentially remove the scatter component entirely if the scatter can be estimated accurately. The scatter correction methods all include two main parts: scatter estimation and scatter correction [9, 10].

The scatter can be estimated using two approaches: Monte Carlo simulation or experimental measurements [10]. The Monte Carlo method is more accurate than the experimental scatter estimation methods at the cost of high computational load. For 2D x-ray imaging, several measurement based methods were developed for scatter correction such as the posterior beam-stop [11] and Fourier deconvolution [12, 13]. In CT or CBCT, several measurement-based methods were developed by using collimator shadow [14], beam stop array [15-18] and primary modulator [19-21] to measure the scatter component or SPR directly for scatter correction:

- i) In the collimator shadow method, a collimator is applied to measure the scatter fluence under the collimator area outside the field of view. The scatter distribution is estimated by interpolation from the boundary data[14].

- ii) In the beam stop array method described by Zhu et al[9], the scatter is measured in a few partially blocked CBCT projections to estimate the scatter distribution in the measured projections by using interpolation/extrapolation. The scatter in the conventional unblocked CBCT projections will be estimated and corrected based on the scatter measured in the partially blocked CBCT projections. Although this method improves the image quality effectively, patients' imaging time and dose is increased substantially due to the need of a separate CBCT scan for scatter estimation. In addition, the scatter estimation from a patient scan with beam blockers may not be accurate for scatter correction of a patient scan without the beam blockers.
- iii) The primary modulator method is based on the hypothesis that scatter distribution has primarily low spatial frequency. The modulation grid, similar to beam stop array but semi-translucent, is applied to perform scatter correction. Although scatter correction methods can potentially remove the scatter effects effectively, they also introduce noise during the scatter correction process. As a result, the CNR may not improve or even degrade after scatter correction. Novel noise suppression methods are being developed for the scatter correction methods through post-processing or improvement of reconstruction algorithms [10, 22].

1.3.3 Combining Scatter Reduction and Correction in a Synchronized Moving Grid (SMOG) System

Jin et al [23] proposed a Synchronized Moving Grid (SMOG) system to combine the effects of scatter reduction and scatter correction. SMOG acquires patient projection images with a grid attached to the x-ray source. The grid divides the cone-beam into multiple quasi-fan beams to provide physical scatter reduction. The patient information is obtained in the unblocked region in the projection, and scatter is measured in the blocked region for post-scan scatter correction. Complete patient projections are achieved by merging complementary partially blocked projections acquired with the grid moved to different locations at each scan angle. Compared to the scatter correction method proposed by Zhu et al [9, 18], SMOG has the following advantages: 1) less imaging dose as SMOG doesn't require a separate scan for scatter estimation, 2) better CNR enhancement due to the physical scatter reduction process in SMOG, 3) more accurate estimation of scatter as SMOG measures the scatter under the same imaging conditions as during patient acquisition, and 4) reduced lag effects allowed by SMOG's unique acquisition scheme, as demonstrated by Ren et al [24].

1.4 Research Aim

The aim of this project is to investigate the usage of the Synchronized Moving Grid (SMOG) system we developed before for scatter suppression on a prototype dual-source CBCT system. The experiments were conducted with different phantom sizes, grid blocking ratios, image acquisition modes and reconstruction algorithms to

investigate their effects on the performance of the SMOG system. The image quality improvement by SMOG was evaluated both qualitatively and quantitatively through contrast-to-noise ratio index (CNR'), HU value accuracy and uniformity.

2. Materials and Methods

2.1 Experiment Equipment

The experiment was designed to implement the scatter suppression method using the SMOG system developed by Ren et al [24]. Here are three main components in this experiment: the in-house developed dual-source CBCT system, the pre-patient 1D grid and the phantom. The pre-patient 1D grid was attached in front of the x-ray tube to implement scatter reduction and scatter correction. The CATphan, containing various structures such as different contrast modules and homogeneous regions, was used in the experiment for the image quality analysis. The details of these three components will be described in the following paragraphs.

2.1.1 Dual-source CBCT System

The dual-source CBCT system built by Giles et al [25] consists of two x-ray tube (Varian G-242, Varian Medical System, Palo Alto, CA) and two flat panel detectors (PaxScan® 4030CB, Varian Medical System, Palo Alto, CA). In this system, both tubes and detectors are fixed and the object being imaged is rotated by the rotational stage to acquire projections at different angles. The distance between each detector and the center of the rotational stage is 50cm, and the distance between each x-ray source and the center of the stage is 100cm, same as the set up in the clinical on-board imager (OBI) system on a Linac. The central rays of two x-ray sources pass the central axis of the stage and are orthogonal to each other, as shown in Figure 2-1. The total filtration for each

tube is 2.7mm Al equivalent. The size of each flat-panel detector is 397×298 mm² with a pixel pitch of 194μm [25].

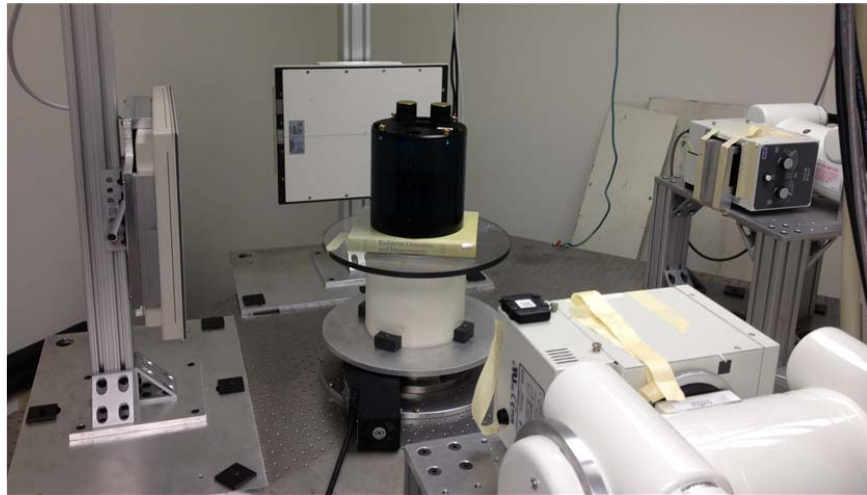


Figure 2-1. The dual-source CBCT system with the CATphan phantom.

2.1.2 Pre-patient Grid

Two types of grids were designed to investigate the effects of grid blocking ratio on the scatter reduction and scatter correction. For each grid blocking ratio as shown in Figure 2-2 and Figure 2-3, two grids made of 95WNI₂Cu tungsten alloy were manufactured for the two x-ray tubes. The grid blocking ratio is defined as the ratio of blocked area and unblocked area. Grid blocking ratios of 1:1 and 2:1 were evaluated in this project. The thickness of each grid is 3.5mm. Using the attenuation coefficient of tungsten at energy of 100 keV, it can be calculated that only 9.00E-14 of initial photon will go through the 3.5 mm thickness grid. Therefore, it's reasonable to assume that no primary photons will go through the blocked area of the grid.

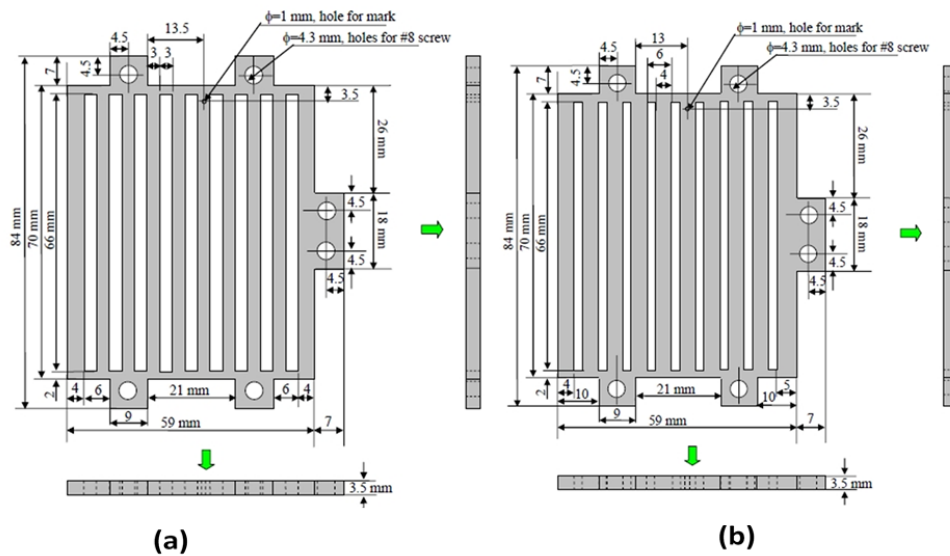
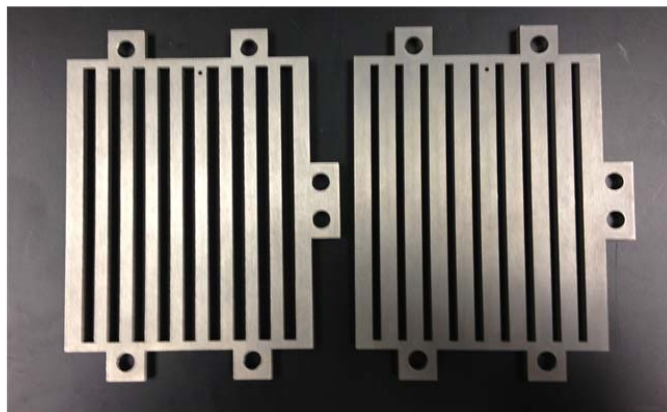


Figure 2-2. Three views of the (a) 1:1 grid and (b) 2:1 grid.



(a) (b)

Figure 2-3. Picture of the (a) 1:1 grid and (b) 2:1 grid.

2.1.3 Phantom

CATphan[®] 504 (as shown in Figure 2-4) commonly used in CT QA was used in this project to evaluate the image quality improvement with scatter reduction and correction technology.

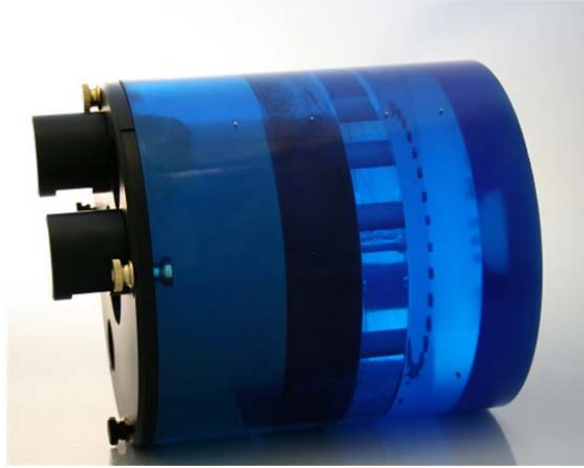


Figure 2-4. Picture of the phantom from the Catphan® 504 Manual.

Four modules are designed in this phantom to test the image quality of CBCT.

The name, consistence and the function of each module are list in Table 2-1

Table 2-1. Name, consistence and the function of each module in Catphan 504.

Module	Detail	Test
CTP404	<ul style="list-style-type: none"> • 10,8,6,4,2mm acrylic spheres • 50mm spaced air and Teflon rods • Sensitometry samples • 23°ramps 	<ul style="list-style-type: none"> • HU verification • Slice thickness • Spatial linearity of pixel size
CTP528	<ul style="list-style-type: none"> • 21 line pair high resolution 	<ul style="list-style-type: none"> • High contrast resolution
CTP515	<ul style="list-style-type: none"> • Subslice and supra-slice low contrast 	<ul style="list-style-type: none"> • Low contrast resolution
CTP486	<ul style="list-style-type: none"> • Solid image uniformity module 	<ul style="list-style-type: none"> • Uniformity • Noise

In addition, the size of the phantom can be changed by adding annuli outside the CATphan. In this project, the diameter of the CTP 404 module varies from 15cm, 20cm and 30cm.

2.2 Experiment Setup

2.2.1 Basic Setup

120 kVp and 1mAs (40mA and 25ms) per projection were used with reference to the conventional parameters of a thorax CBCT scan in the clinic. Bowtie filters, as shown in Figure 2-5, were attached to both x-ray sources during the scan. The imaging dose will be reduced with the bowtie as it will attenuate the unnecessary x-ray close to the peripheral of the body. Mail et al [26] also showed that the bowtie filter on a CBCT System improved the CT number accuracy, image uniformity and contrast by reducing the fluence variation on the detector.

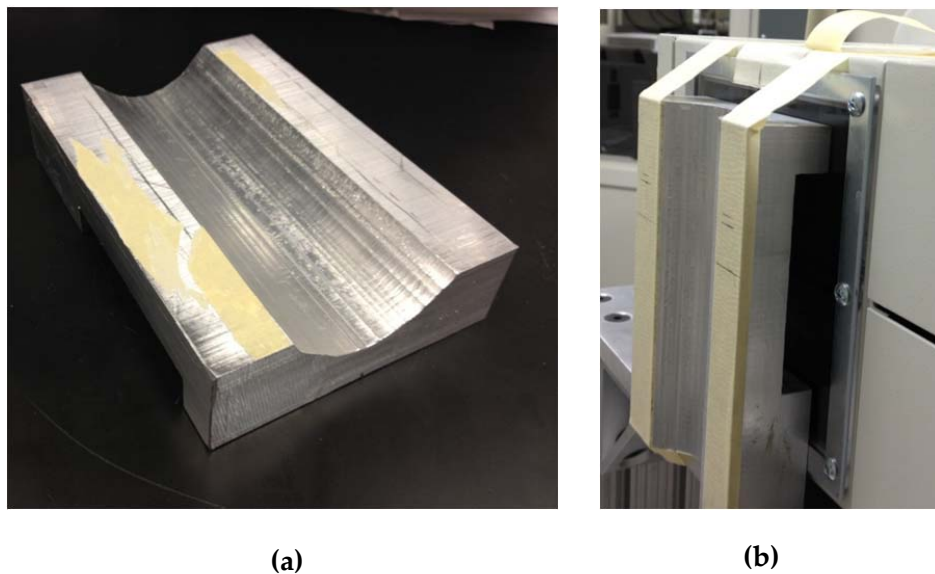


Figure 2-5. Picture of the bowtie for the full fan scan. (a): Bowtie filter. (b): Bowtie attached on the tube.

The experiment set up is shown in Figure 2-6 and Figure 2.7. The bowtie filter was fixed on the tube. The grids for the scatter reduction and correction were placed on

the top of the bowtie filters and moved manually after one rotation scan to acquire complementary projections at each angle. The distance between grid and x-ray focal spot is 27cm. In our study, grids were attached close to the x-ray source so that they can cover the entire imaging field.

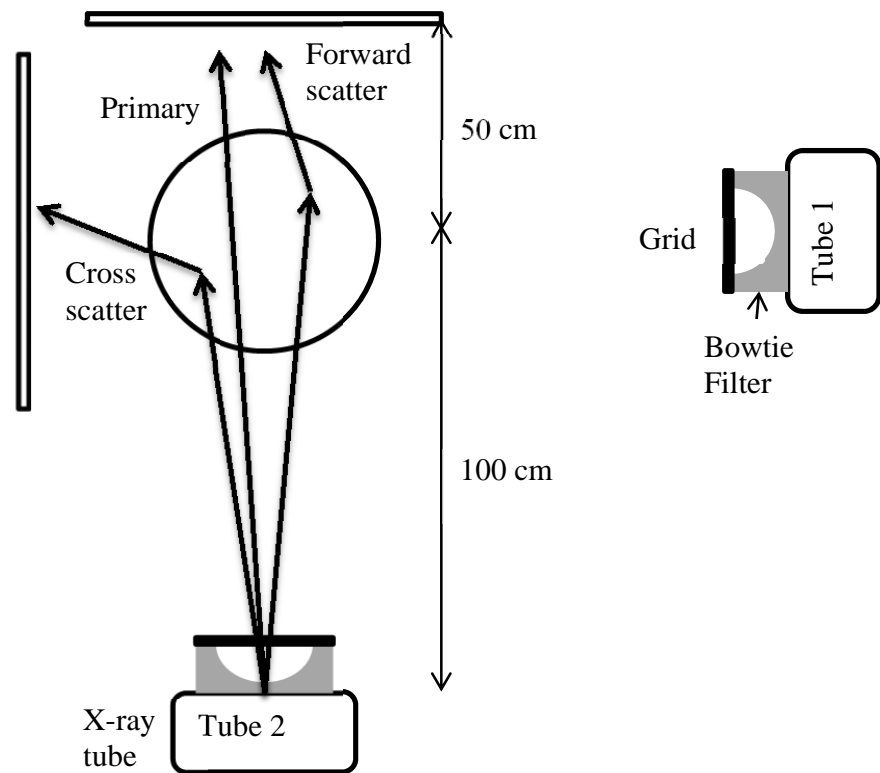


Figure 2-6. Schematic diagram of the SMOG system in the dual-source CBCT system. Both the forward scatter and the cross scatter will reach the detector. Grid is put between the patient and the tube.

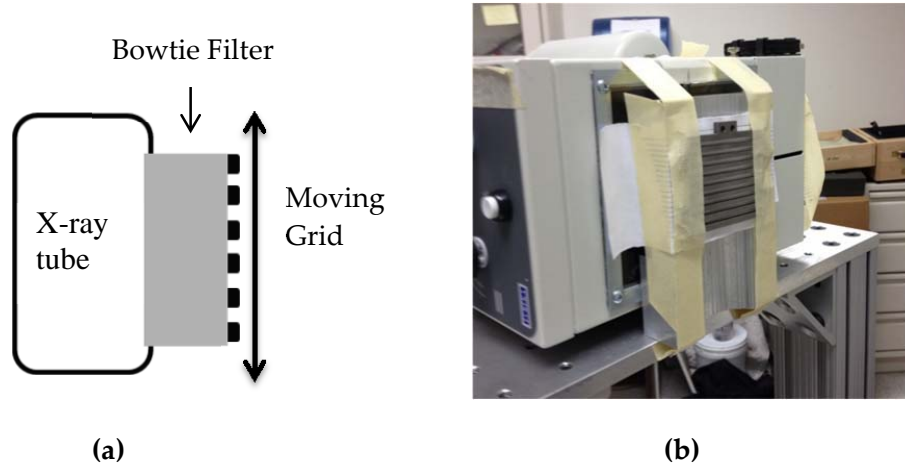


Figure 2-7. Diagram of the x-ray source. (a) Left sagittal view of the source. (b)

Image of the bowtie filter and the grid attached to the source.

2.2.2 Acquisition Mode

Based on the design of the in-house developed dual-source CBCT system, three acquisition modes as described in [25] (simultaneous mode, interleaved mode and sequential mode) were used in our experiment. In the simultaneous mode, the two x-ray tubes fire simultaneously and the two detectors record at the same time at each scan angle during a one-rotation scan. In the interleaved acquisition mode, the tubes fire alternatively while two detectors record all the time even when their corresponding tube is not firing. In the sequential mode, only one tube fires and its corresponding detector records images in one rotation. Then, the other set of tube and detector acquires in the next rotation. Cross scatter of dual-source CBCT system were investigated by these three acquisition modes.

2.2.3 Data Description

720 empty and phantom projections were acquired over a 360 degree scan angle with frame rate equal to 4 f/s. For each exposure, 120kVp and 1mAs was chosen. Several experiments were conducted using various settings: different phantom sizes (diameter: 15cm, 20cm and 30cm), different grids (grid blocking ratios of 1:1 and 2:1) and acquisition modes (simultaneous, interleaved and sequential). Table 2-2 lists all imaging conditions used in this project.

Table 2-2. Experimental conditions investigated in the study.

Phantom Size: Diameter (cm)	Grid	Acquisition Mode
15	1:1	Simultaneous
		Interleaved
		Sequential
	Without grid	Simultaneous
		Interleaved
		Sequential
20	1:1	Simultaneous
		Sequential
	2:1	Simultaneous
		Interleaved
		Sequential
	Without grid	Simultaneous
		Sequential
		Interleaved
	30	1:1
Sequential		
Without grid		Simultaneous
		Sequential

2.3 Scatter Correction Algorithm

The grid-based scatter correction method used in this project is the same as that described by Ren et al [23, 27]. In order to obtain the complete projections of the object,

complementary projections were acquired at each angle with the grid offset by a distance equal to the grid interspace after each exposure. Due to the lack of a motor to automatically move the grid, the grid was static during each full rotation scan, and was manually moved in-between scans in our experiments. The number of the scans needed is determined by the grid blocking ratio. For example, the 1:1 grid blocks half of the x-ray beam in each projection and two projections need to be acquired at each angle to obtain complete information. As a result, two scans are needed with the grid off set in-between scans. Complete projection images are obtained by merging the scatter-corrected complementary projections acquired at different grid positions.

The grid-based scatter correction algorithm is implemented in five steps: (1) acquire empty scan (without phantom) and phantom scan with grids; (2) Estimate the scatter distribution based on the measured scatter data from blocked areas in each empty scan and phantom scan projection using a cubic spline interpolation/extrapolation along the longitudinal direction; (3) Subtract the scatter distribution from projection images for scatter correction; (4) Negative logarithm transformation of the division of the scatter-corrected phantom scan projections and the corresponding scatter-corrected empty scan projections; (5) Merge the projections obtained in step 4 to obtain complete scatter corrected projections. The general process of the scatter correction algorithm is shown in Figure2-8 using the example of a 1:1 grid.

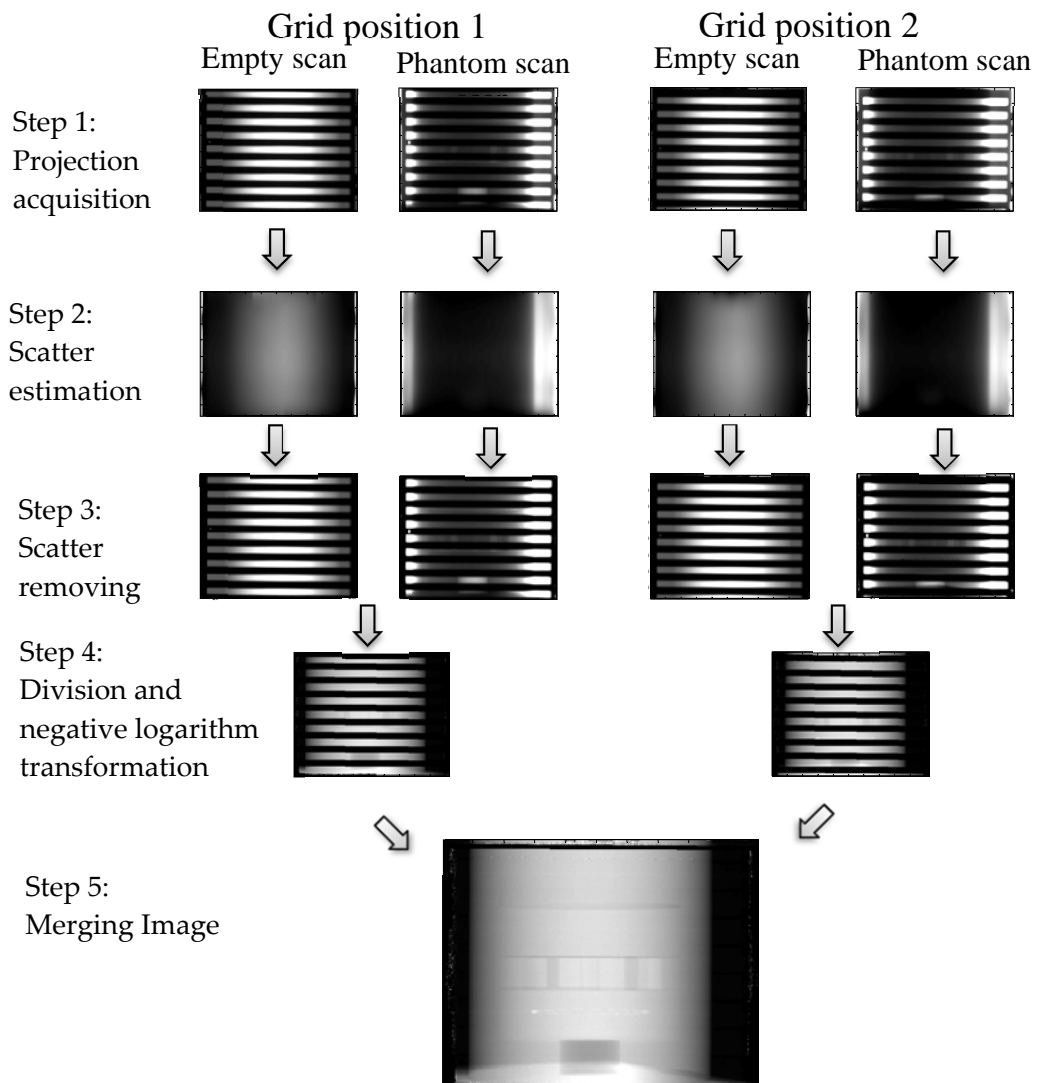


Figure 2-8. An example to illustrate the scatter correction procedure using 1:1

grid.

The profiles of the center column in a projection image are shown in Figure2-9 and Figure 2-10, to illustrate the scatter measurement, estimation and removal process for empty scan and phantom scan projections.

(a) Profile of empty scan projection (before and after correction)

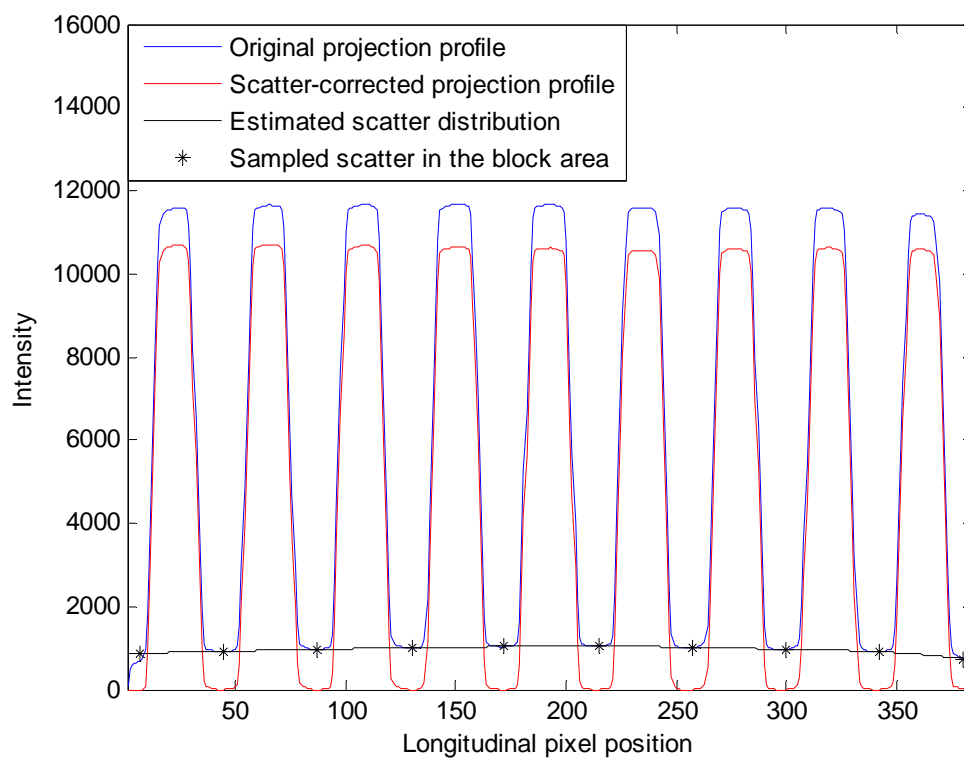


Figure 2-9. An example illustrating the scatter estimation and correction process in an empty scan. The blue solid line is original 1 D profile in the longitudinal direction in an empty scan projection. The star dots are the measured scatter in the blocked areas. The black line is the interpolated scatter distribution. The red solid line is final profile after scatter correction by subtracting the black line from the blue line.

(b) Profile of phantom projection (before and after correction)

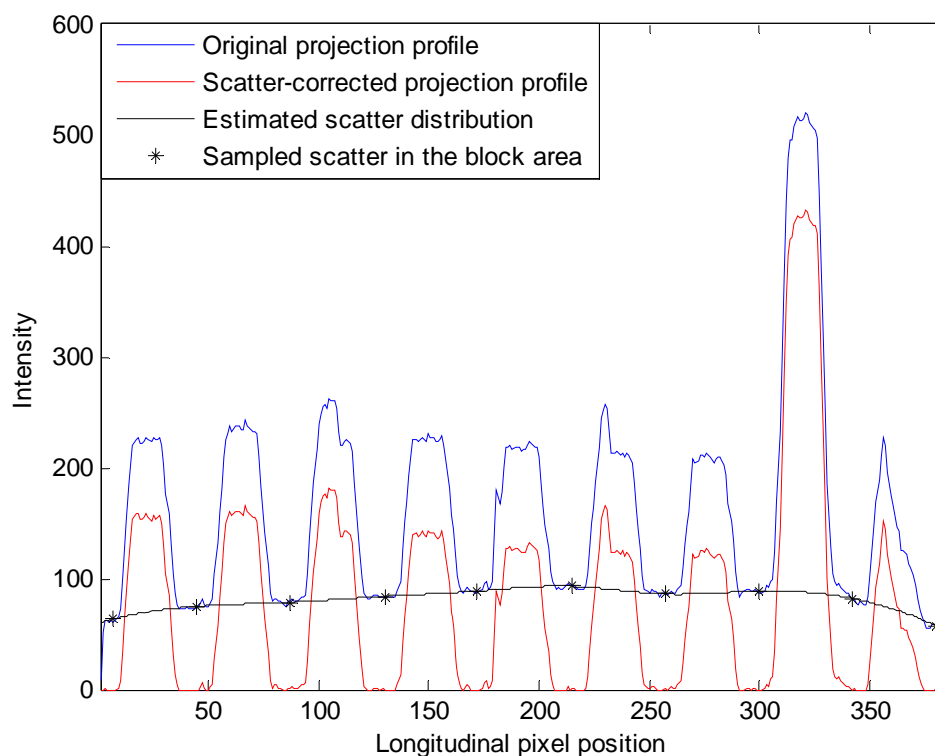


Figure 2-10. An example illustrating the scatter estimation and correction process in a phantom scan. The blue solid line is original 1 D profile in the longitudinal direction in a phantom scan projection at a specific angle. The star dots are the measured scatter in the blocked area. The black line is interpolated scatter distribution. The red solid line is final profile after scatter correction by subtracting the black line from the blue line.

The process of merging the images acquired with different grid positions is shown in Figure 2-11. After the negative logarithm transformation of the division

between the scatter-corrected phantom scan projections and the corresponding scatter-corrected empty scan projections, complementary partially blocked projections were added together to obtain a complete projection at a scan angle. Note that average values were used in the overlapping data regions between the complementary projections. This process was repeated for different scan angles to obtain a complete set of scatter corrected projections for CBCT reconstruction.

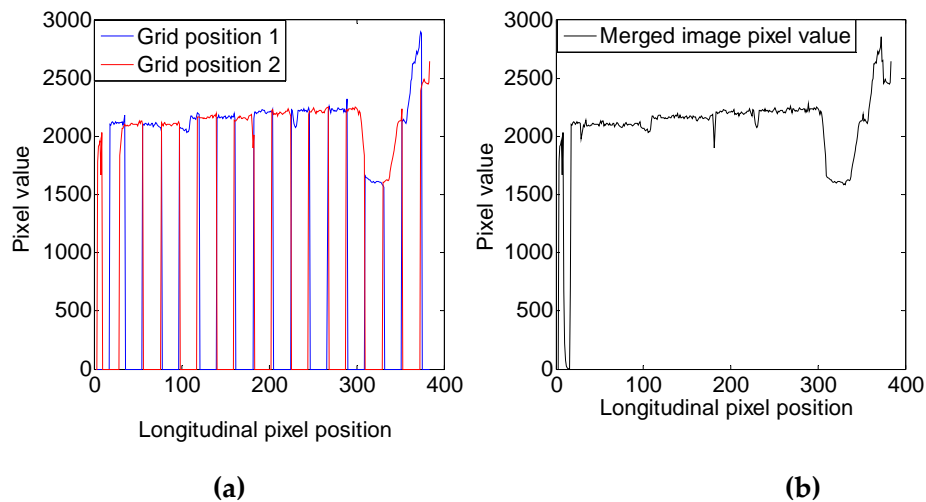


Figure 2-11. Profiles extracted from complementary projections after empty scan normalization and negative logarithm transformation. (a) The red and blue solid lines were from two complementary projections acquired with the grid shifted by one grid inter-space. (b) Profile of the merged projection.

The effects of scatter reduction only can be studied using the partially blocked projections directly for reconstruction without the scatter correction process. Basically, the scatter reduction only method uses the same process shown in Fig. 2-8 except skipping step 2 and step 3.

2.4 Reconstruction Algorithm

Different reconstruction algorithms have been developed for CBCT reconstruction. One commonly used method is the Feldkamp, Davis, and Kress (FDK) back projection method [28], which has a high efficiency for reconstruction. Other types of reconstruction include different iterative algorithms, such as iterative reconstruction based on a maximum-likelihood (ML) principle [29] or total variation (TV) minimization [30, 31]. These methods were developed to improve reconstruction using incomplete data or reduce the noise in low-dose CT. Compared to FDK method, iterative methods have longer reconstruction time and require higher computing power.

In this study, FDK and the in-house-developed iterative reconstruction method with total variation (TV) minimization were used to evaluate the influence of reconstruction method on the scatter correction.

2.5 Image Quality Assessment

The effectiveness of scatter reduction and scatter correction was analyzed both qualitatively and quantitatively in this project. The methods used to assess scatter artifact, contrast to noise ratio index (CNR'), CT number linearity and uniformity will be discussed in the following sections.

2.5.1 Qualitative Assessment on Artifact

From the previous studies, cupping and streak artifacts are usually caused by scatter and beam hardening [3, 32]. Using the Catphan 504 phantom, scatter artifact was evaluated in the images of CTP404 module visually.

2.5.2 Contrast-to-noise Ratio Index (CNR')

Scatter radiation will degrade the low contrast detectability. Contrast-to-noise ratio index (CNR') was measured for each insert in the images of CTP404 module to evaluate the contrast and noise in the image. The regions of interests (ROIs) were drawn in the circulars (about 50 pixels as shown in Figure 2-12). Red circles were drawn in the inserts, and yellow circles were drawn adjacent to the inserts to evaluate the pixel values for CNR' calculation. The calculation formula is as follows:

$$CNR' = \frac{|\bar{N} - \bar{N}_0|}{(\sigma + \sigma_0)/2} (1)$$

Where \bar{N} and σ are the mean value and the standard deviation of the pixel value in the ROI of the insert while \bar{N}_0 and σ_0 is calculated from the ROI outside the insert.

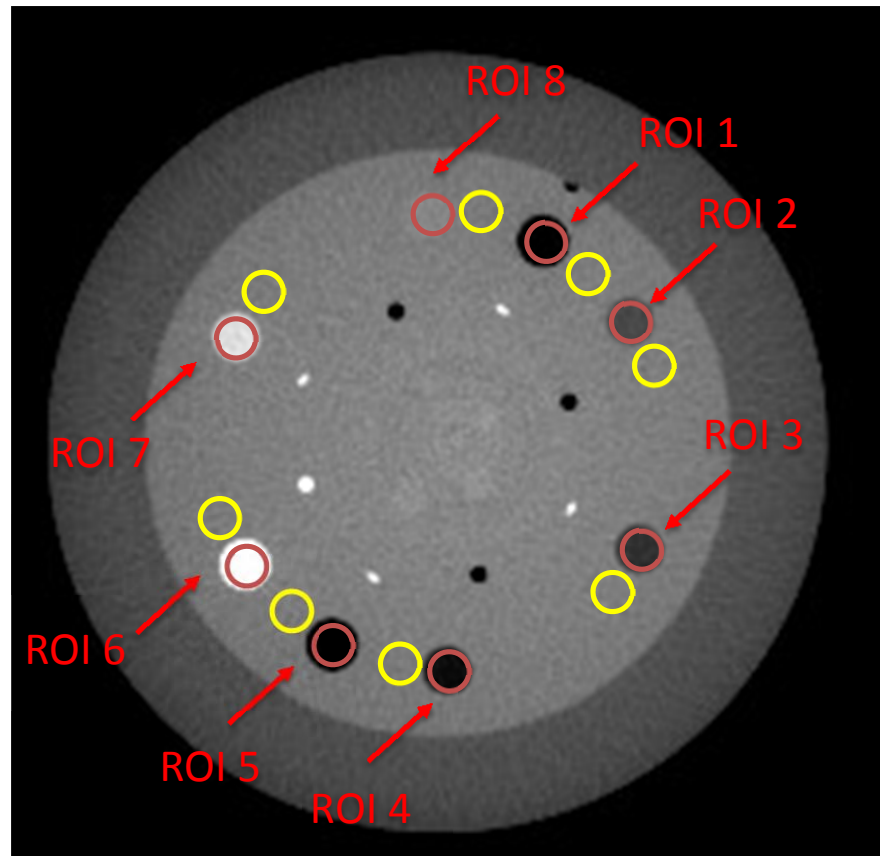


Figure 2-12. Axial view of the CTP404 module with eight different inserts reconstructed by the FDK method. The red circles are the ROIs inside the inserts while the yellow ones are the ROIs surrounding the inserts.

2.5.3 HU Number Linearity

The Hounsfield unit (HU) number, widely used in the radiology, is calculated from pixel value in the reconstructed image. Linear regression was performed between all mean values of the eight inserts shown in Figure 2-12 and their corresponding nominal CT number shown in Figure 2-13. CT number linearity was evaluated by the regression coefficients R^2 . Higher R^2 indicates better linearity.

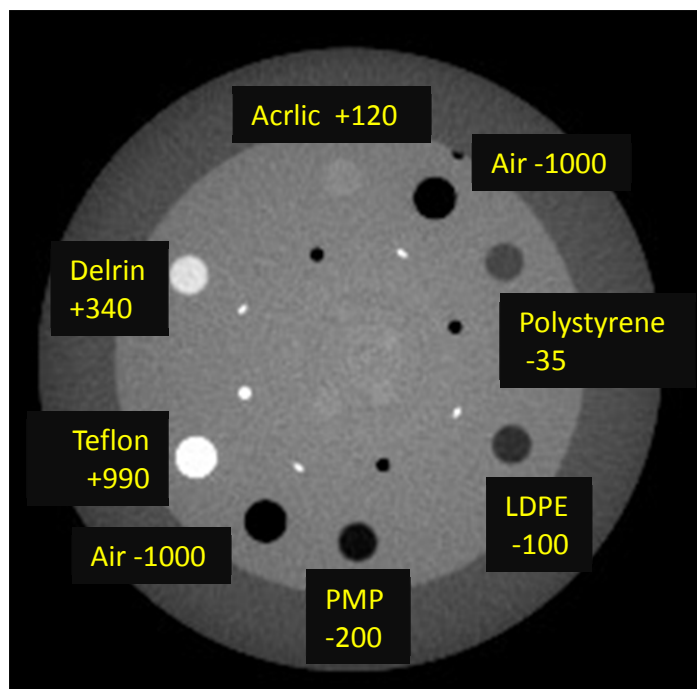


Figure 2-13. Nominal HU values of the eight inserts in the CTP404 module.

2.5.4 Uniformity

Uniformity was evaluated on the uniformity slices of the CatPhan. The mean values of the five ROI (20*20 pixels), located in the center and boundary of the phantom are shown in Figure 2-14. The uniformity index was achieved by calculating the

standard deviation of five ROI mean values to evaluate the difference between the CT number of center and the peripheral regions.

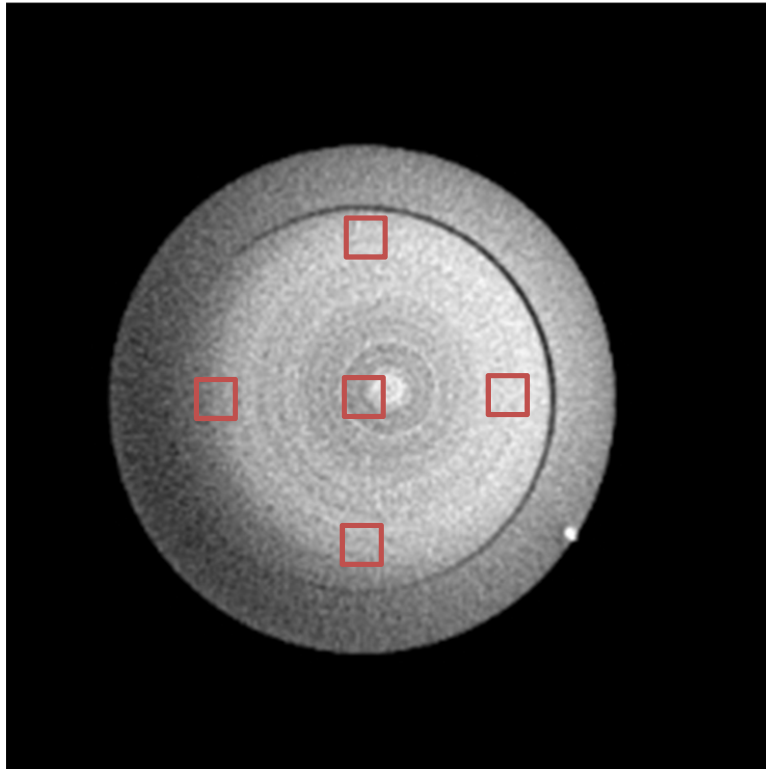


Figure 2-14. Axial view of the CTP486 uniformity module of the CATphan. Five ROIs were defined (one is in the center and the other four are at the edge) to calculate the uniformity of the image.

3. Results

3.1 Scatter Artifact, Scatter Reduction and Correction

Three images set were reconstructed from projections (a) without grid (**original images**), (b) with grid and without scatter correction (**scatter reduction only**) and (c) with grid and with scatter correction (**scatter reduction and correction**) for different parameter settings, as discussed in the method section.

Different acquisition modes (simultaneous, interleaved and sequential)

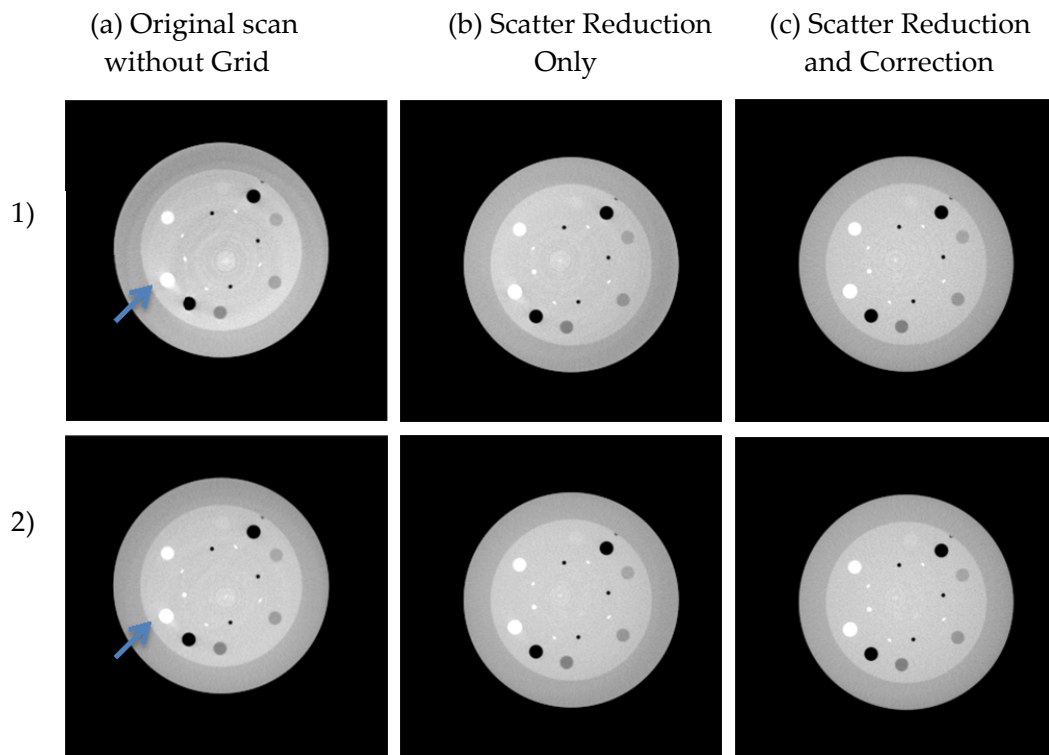


Figure 3-1. Reconstructed images of a CATphan of 20cm diameter using 1) simultaneous and 2) sequential acquisition mode. 1:1 grid was applied for scatter reduction and scatter correction. From left to right column: (a) without grid, (b) scatter reduction only and (c) scatter reduction and correction. Window width of 1000HU and window level of -200HU were used for all images.

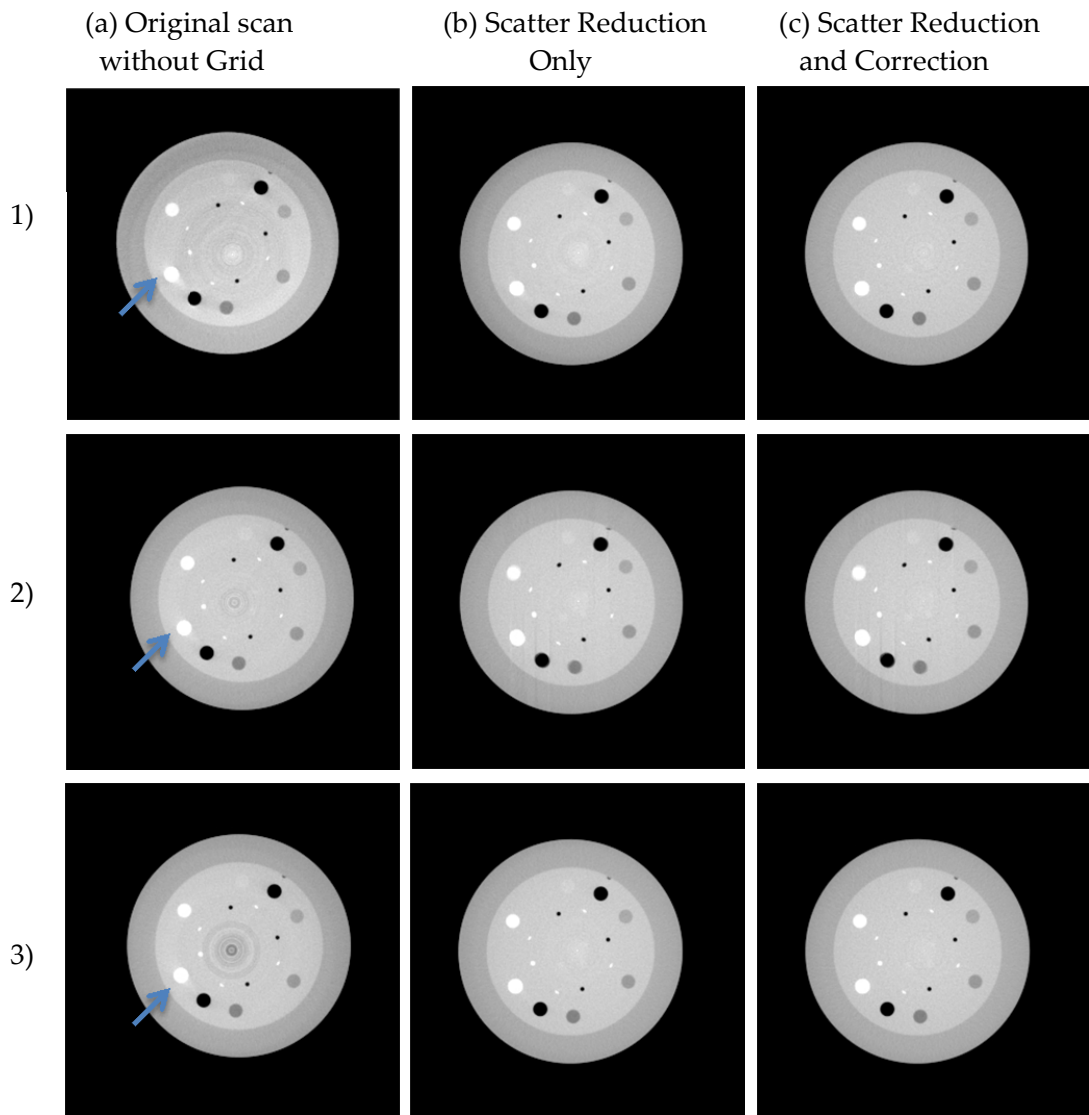


Figure 3-2. Reconstructed images of a CATphan of 20cm diameter using 1) simultaneous, 2) interleaved and 3) sequential acquisition mode. 2:1 grid was applied for scatter reduction and scatter correction. From left to right column: (a) without grid, (b) scatter reduction only and (c) scatter reduction and correction. Window width of 1000HU and window level of -200HU were used for all images.

CATphan with different diameters (15, 20, 30cm)

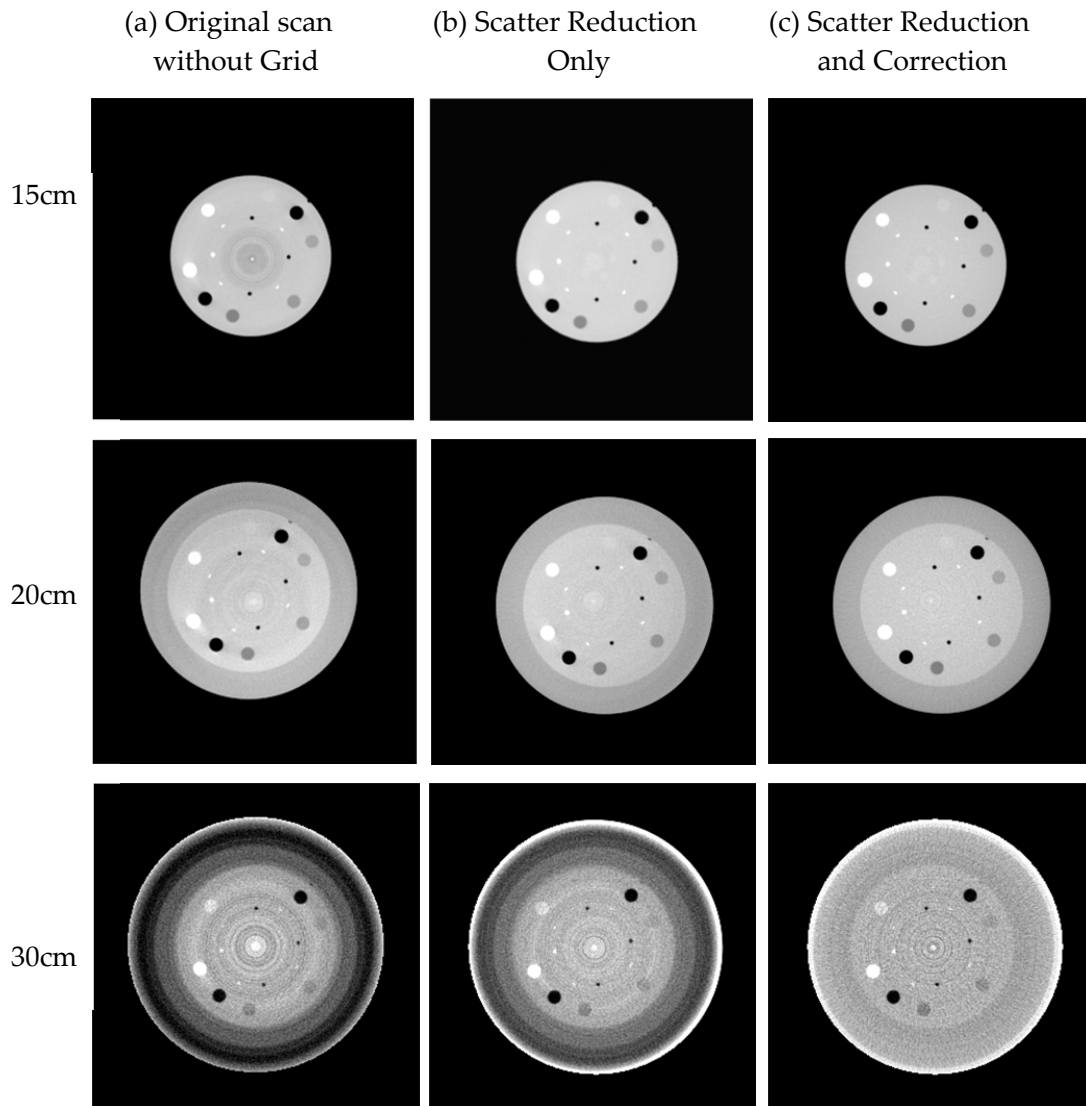


Figure 3-3. Reconstructed images of a CATphan of 15, 20 and 30cm diameters (from 1st to 3rd row) acquired by simultaneous mode (dual-source). 1:1 grid was applied for scatter reduction and scatter correction. From left to right column: (a) without grid, (b) scatter reduction only and (c) scatter reduction and correction. Display for 1st and 2nd: window width of 1000HU and window level of -200HU were used. Display for 3rd: window width of 2200HU and window level of 100HU were used.

Different grids (grid blocking ratios of 1:1 and 2:1)

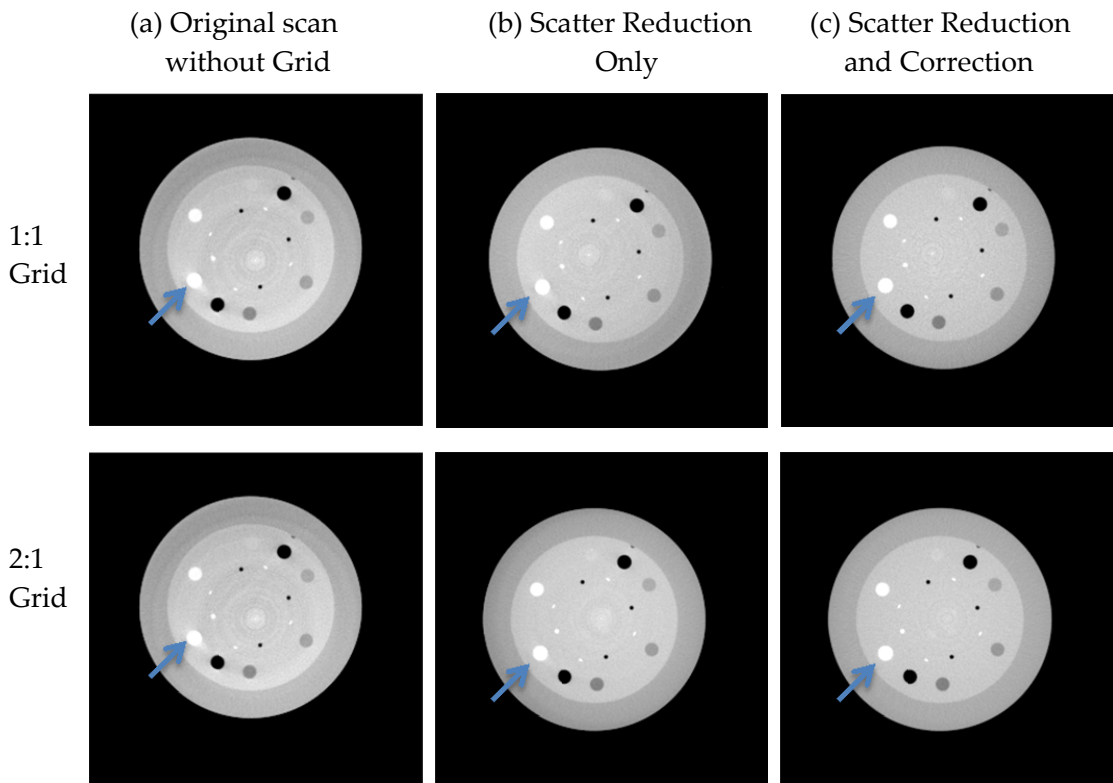


Figure 3-4. Reconstructed images of a CATphan of 20 cm diameter acquired by simultaneous mode (dual-source). 1:1(1st row) and 2:1grid (2nd row) was applied for scatter reduction and scatter correction. From left to right column: (a) without grid, (b) scatter reduction only and (c) scatter reduction and correction. Window width of 1000HU and window level of -200HU were used for all images.

As shown from Figure 3-1 to Figure 3-4, scatter artifacts as the arrows pointed seen in the original images are reduced in the scatter reduction only images, and are removed in the scatter reduction and correction images.

Reconstruction algorithm (FDK vs. iterative with total variation)

The results above were generated by FDK reconstruction algorithm. Noise was increased in the scatter correction process, degrading the CNR' especially for large phantom. The noise will be reduced by the iterative reconstruction method as shown in Figure 3-5.

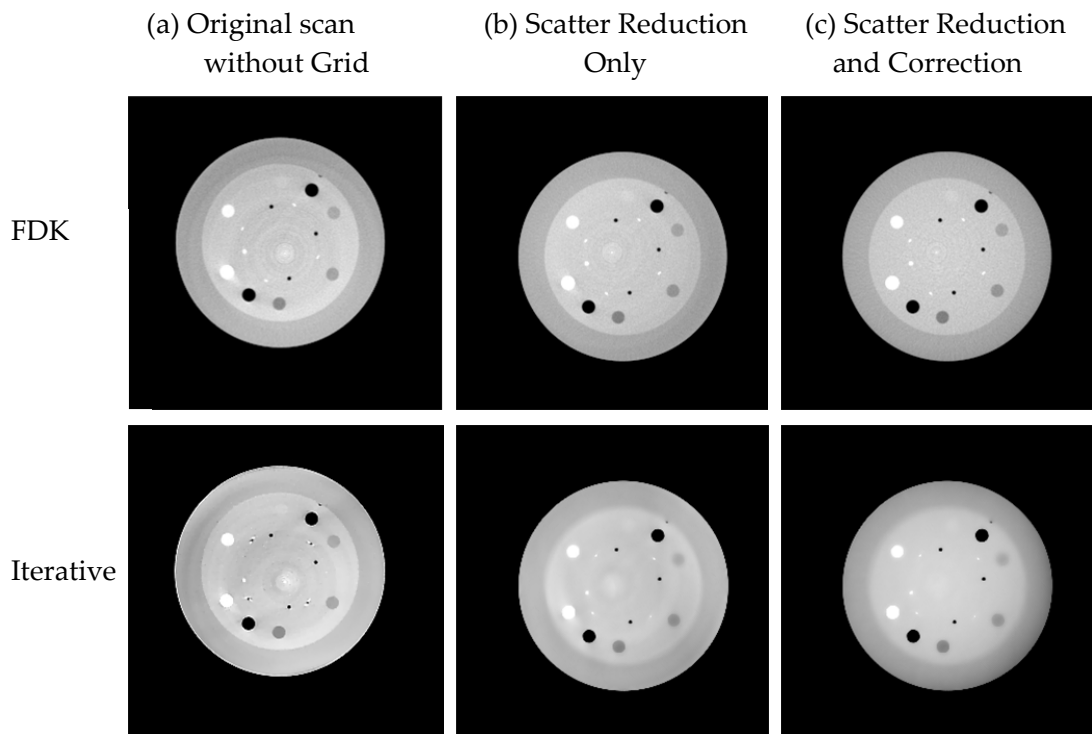


Figure 3-5. Reconstructed images of a CATphan of 20cm diameter acquired by simultaneous mode (dual-source). 1:1 was applied for scatter reduction and scatter correction. Images were reconstructed from the FDK method (1st row) and iterative method (2nd row). From left to right column: (a) without grid, (b) scatter reduction only and (c) scatter reduction and correction. Window width of 1000HU and window level of -200HU were used for all images.

In summary, the results above showed that the scatter artifact was removed by the scatter correction algorithm with grid. Cross scatter increased scatter in the dual-

source CBCT system and degraded image quality with severe artifacts. The grid effect demonstrated in Figure 3-4 showed that high grid blocking ratio (more blocked area) reduced more scatter physically with less scatter artifacts. Scatter artifacts were worse in the larger phantom due to the increase of scatter. Our study also showed iterative reconstruction with total variation regularization would reduce some noise caused by the scatter correction algorithm.

3.2 Contrast-to-noise Ratio Index (CNR')

CNR' of different contrasts in the center slice of the CTP 404 module were calculated using the method described in the Chapter 2 section 2.5.2 for three image sets (original, scatter reduction only, scatter reduction and correction) and different imaging parameters.

Scatter reduction and correction

CNR' of 8 inserts in the axial image of 20cm phantom is shown in Table 3-1. Simultaneous acquisition mode and 1:1 grid were applied in this data set. In most cases, CNR' was increased by using the scatter correction, especially for high contrast inserts. However, CNR's for some inserts decreased for scatter correction strategy as compared to the scatter reduction only strategy, showing the scatter correction may degrade the CNR' by adding more noise via scatter correction process.

Table 3-1. Comparison between CNR' of 8 inserts in three image sets: original CBCT, CBCT reconstructed with scatter reduction only and CBCT reconstructed with scatter reduction and correction. Phantom of 20cm diameter, 1:1 grid and simultaneous mode were used in the scan.

CNR' (20 cm phantom, 1:1 grid, simultaneous mode)			
ROI	Original Data	Scatter Reduction Only	Scatter Reduction and Correction
1	53.4	63.5	66.9
2	8.8	10.1	9.14
3	12	13	12.1
4	15.8	16.9	16.3
5	46.6	56.6	69.2
6	48.5	50	57.5
7	14.4	18.5	18.1
8	3	2.99	2.01

Cross scatter

The CNR' of insert 1 (Air, -1000HU), insert 2 (Polystyrene,-35 HU), insert 6 (Teflon, 990HU) and insert 7 (Delrin, 340HU), containing high- and low- contrast inserts, were used to show the cross scatter effect by using single source or dual source acquisition mode. As shown in Table 3-2 and 3-3, the cross scatter in the simultaneous mode degraded the CNR'. CNR' in the dual-source acquisition mode was increased with scatter reduction and correction algorithm and was comparable to the results from single source scanning mode. Interleaved acquisition can reduce the scatter by largely removing .cross scatter to achieve similar CNR' as a conventional CBCT system [25].

Table 3-2. Comparison between CNR' in images acquired by the simultaneous and sequential scanning modes. Phantom of 20cm diameter and 1:1 grid was used in the scan.

CNR' (20 cm phantom, 1:1 grid)				
ROI	Acquisition Mode	Original Data	Scatter Reduction Only	Scatter Reduction and Correction
1	Simultaneous	53.4	63.5	66.9
	Sequential	72.6	82.6	80.2
2	Simultaneous	8.8	10.1	9.1
	Sequential	9.1	9.2	9.4
6	Simultaneous	48.5	50.0	57.5
	Sequential	56.2	58.6	58.2
7	Simultaneous	14.4	18.5	18.1
	Sequential	16.6	18.9	17.9

Table 3-3. Comparison between CNR' acquired by simultaneous, interleaved and sequential modes. Phantom of 20cm diameter and 2:1 grid was used in the scan.

CNR' (20 cm phantom, 2:1 grid)				
ROI	Acquisition Mode	Original Data	Scatter Reduction Only	Scatter Reduction and Correction
1	Simultaneous	58.3	95.0	95.4
	Interleaved	89.7	97.6	101.7
	Sequential	77.2	97.0	97.4
2	Simultaneous	9.9	12.6	12.4
	Interleaved	10.7	12.3	12.4
	Sequential	11.6	12.2	12.0
6	Simultaneous	37.8	64.8	55.6
	Interleaved	60.3	66.4	68.5
	Sequential	58.3	81.9	73.8
7	Simultaneous	14.9	21.9	20.0
	Interleaved	19.1	21.5	19.4
	Sequential	21.4	21.6	20.4

Phantom size (15, 20 and 30cm)

CNR' of the four inserts were calculated to evaluate the scatter reduction and correction for various phantom sizes as shown in Table 3-4. CNR' is decreased for larger phantom because more scatter is generated from larger phantom. In addition, in small phantom cases, CNR' is increased dramatically after scatter reduction and correction.

Table 3-4. Comparison between CNR' in CBCT images acquired by various phantom sizes.

CNR' (15, 20 and 30cm phantom, simultaneous mode, 1:1 grid)				
ROI	Phantom Size: Diameter (cm)	Original Data	Scatter Reduction Only	Scatter Reduction and Correction
1	15	73.9	122.4	182.6
	20	53.4	63.5	66.9
	30	12.1	16.4	14.5
2	15	20.3	21.5	20.6
	20	8.8	10.1	9.1
	30	1.1	2.0	1.7
6	15	95.6	102.1	99.8
	20	48.5	50.0	57.5
	30	8.2	12.2	10.4
7	15	32.2	38.7	32.3
	20	14.4	18.5	18.1
	30	2.99	3.4	2.96

Grid effect

CNR's of the four inserts were calculated to evaluate the scatter reduction and correction for 1:1 and 2:1 grid acquired in the simultaneous acquisition mode as shown in Table 3-5.

Table 3-5. Comparison between CNR' in CBCT images acquired with different grid blocking ratios (1:1 and 2:1 grids).

CNR' (20 cm phantom, simultaneous mode, 1:1 and 2:1 grid)				
ROI	Grid Blocking Ratio	Original Data	Scatter Reduction Only	Scatter Reduction and Correction
1	1:1	53.4	63.5	66.9
	2:1	58.3	95.0	117.6
2	1:1	8.8	10.1	9.1
	2:1	9.9	12.6	11.7
6	1:1	48.5	50.0	57.5
	2:1	37.8	64.8	66.6
7	1:1	14.4	18.5	18.1
	2:1	14.9	21.9	21.3

Reconstruction algorithm (FDK vs. iterative with total variation (TV))

Similar to previous section, the CNR's of the four inserts were calculated to evaluate the FDK and iterative with TV reconstruction methods as shown in Table 3-6.

Table 3-6. Comparison between CNR' in CBCT images reconstructed by the FDK and iterative method.

CNR' (20 cm phantom, simultaneous mode, 1:1 grid)				
ROI	Reconstruction Method	Original Data	Scatter Reduction Only	Scatter Reduction and Correction
1	FDK	53.4	63.5	66.9
	TV	74.4	84.5	117.0
2	FDK	8.8	10.1	9.1
	TV	20.6	9.1	9.4
6	FDK	48.5	50.0	57.5
	TV	57.5	67.0	91.2
7	FDK	14.4	18.5	18.1
	TV	23.5	21.6	22.5

3.3 HU Number Linearity

R^2 (regression coefficients) between mean ROI pixel value and the nominal HU value of 8 inserts were calculated as shown in Table 3-7 for various settings.

Table 3-7. Regression coefficients R^2 between reconstructed and nominal HU values for various experimental settings.

Phantom Size	Grid	Acquisition Mode	Original Data	Scatter Reduction Only	Scatter Reduction and Correction
15	1:1	Simultaneous	0.9995	0.9997	0.9998
		Interleaved	0.9998	0.9998	0.9999
		Sequential	0.9997	0.9998	0.9999
20	1:1	Simultaneous	0.9969	0.9989	0.9997
		Sequential	0.9991	0.9995	0.9998
	2:1	Simultaneous	0.9983	0.9985	0.9999
		Interleaved	0.9994	0.9995	0.9999
		Sequential	0.9993	0.9994	0.9999
30	1:1	Simultaneous	0.9933	0.9915	0.9993
		Sequential	0.9967	0.9971	0.9998

Results showed slight improvement of R^2 , which indicates the linear relationship between reconstructed HU and nominal HU. The reconstructed HU after HU scale was calculated for the 20cm phantom with 1:1 grid, as shown in table 3-8 and Figure 3-6. The results showed that reconstructed HU number and nominal HU number were linearly correlated and HU accuracy was improved slightly with our method.

Table 3-8. HU accuracy in reconstructed CBCT images of the 20cm-diameter phantom acquired with the 1:1 grid and the simultaneous scanning mode.

ROI	Nominal HU	Reconstructed HU		
		Original	Scatter Reduction	Scatter Reduction and Correction
1	-1000	-1040.7	-1008	-998.623
2	-35	-23.2	-59.2	-52.1574
3	-100	-43.8	-119.5	-112.711
4	-200	-148.4	-190.7	-198.119
5	-1000	-1005.6	-992	-992.3
6	990	959.9	970.6	991.128
7	340	319.7	378.8	356.1206
8	120	97.2	134.9	121.6618

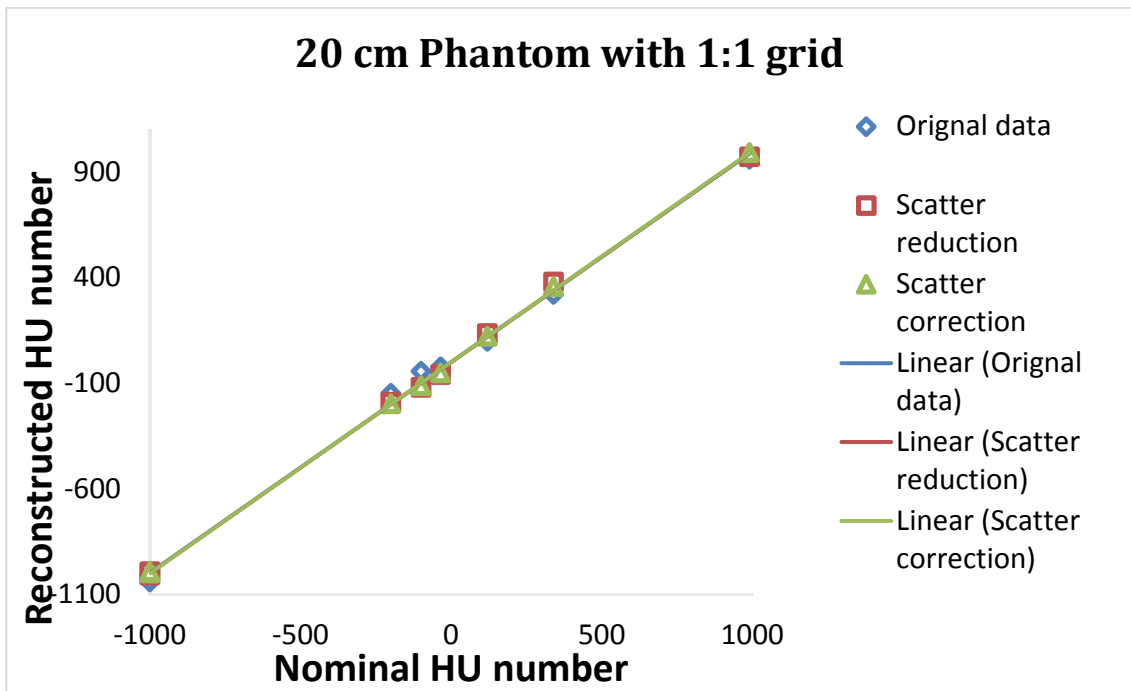


Figure 3-6. Plot of the reconstructed HU value for each ROI vs. nominal HU values are shown for the 20cm-diameter phantom for different scatter reduction and correction techniques.

3.4 Uniformity

The uniformity index, as seen in Table 3-9, was calculated by using the standard deviation of the mean value of 5 ROIs described in the Chapter 2. In addition, corresponding axial images of the uniformity module are shown in Figure 3-7. Our method can improve the uniformity by removing some cupping or capping artifacts.

Table 3-9. Uniformity index of three image sets: original CBCT, CBCT reconstructed with scatter reduction only and CBCT reconstructed with scatter reduction and correction. The phantom of 20 cm diameter, 1:1 grid and simultaneous mode were used in this scan.

Uniformity Index		
Original Data	Scatter Reduction Only	Scatter Reduction and Correction
27.71	17.18	9.49

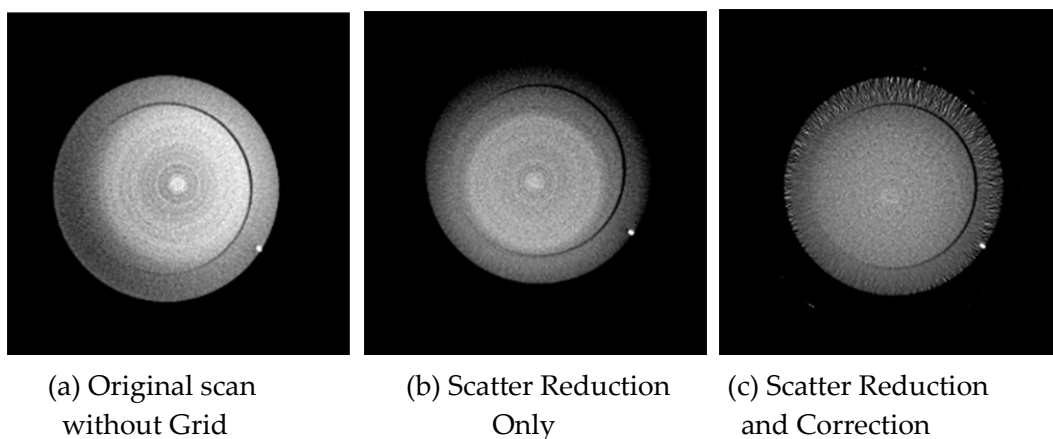


Figure 3-7. Reconstructed images of a CATphan of 20cm diameter (CTP 486: uniformity module) acquired by simultaneous mode (dual-source). 1:1 grid was applied for scatter reduction and scatter correction. From left to right: (a) without grid, (b) scatter reduction only and (c) scatter reduction and correction. Window width of 250HU and window level of 25HU were used for three images.

4. Discussion

4.1 Scatter Reduction and Scatter Correction with Various Experimental Settings

Scatter artifact were reduced by scatter reduction, and were removed by the scatter correction method. As the results shown in Table 3-1 for 20cm phantom, scatter reduction alone enhances the CNR', while adding scatter correction may enhance or degrade CNR' due to the increase of noise in the scatter subtraction process.

The following mathematical derivation was performed in order to quantitatively illustrate the increase of noise with scatter reduction and correction. Assuming there is only Poisson noise in the image [22], the variables used here are listed as follows:

s: detected scatter signal in the phantom scanned without grid, mean value: S

p: detected primary signal in the phantom scanned without grid, mean value P

s₀: detected scatter signal in the empty scan without grid, mean value S₀

p₀: detected primary signal in the empty scan without grid, with mean value P₀

g: grid blocking ratio

q: projection image after empty scan normalization and -log transformation
acquired without grids

q_c: projection image after empty scan normalization and -log transformation
acquired with grids and scatter correction

Since s, p and s₀ and p₀ are Poisson distribution. We also assume s and p are independent, thus, s+p is also Poisson distribution.

Due to Poisson distribution statistics,

$$\text{var}(s) = S, \text{var}(p) = P, \text{var}(s_0) = S_0, \text{var}(p_0) = P_0. \quad (2)$$

Based on the definition, q is expressed as following:

$$q = \ln\left(\frac{s_0 + p_0}{s + p}\right) \quad (3)$$

The scatter photons will be reduced by the 1D blocking grid physically because partial primary photons are blocked. Thus, when the grid is applied, the detected scatter signal will be reduced to $1/(g+1)$ of scatter signal acquired without grids. We also represent the estimated scatter values as $S_0/(g+1)$ and $S/(g+1)$ in the empty and phantom projection, respectively. Similarly, q_c can be written as:

$$q_c = \ln\left[\frac{\left(\frac{1}{g+1}\right)s_0 + p_0 - \left(\frac{1}{g+1}\right)S_0}{\left(\frac{1}{g+1}\right)s + p - \left(\frac{1}{g+1}\right)S}\right] \quad (4)$$

Based on the error propagation formula, the variance of q and q_c is approximated as:

$$\begin{aligned} \text{var}(q) &= \left(\frac{\partial q}{\partial s_0}\right)^2 \text{var}(s_0) + \left(\frac{\partial q}{\partial p_0}\right)^2 \text{var}(p_0) + \left(\frac{\partial q}{\partial s}\right)^2 \text{var}(s) + \left(\frac{\partial q}{\partial p}\right)^2 \text{var}(p) \\ \text{var}(q_c) &= \left(\frac{\partial q_c}{\partial s_0}\right)^2 \text{var}(s_0) + \left(\frac{\partial q_c}{\partial p_0}\right)^2 \text{var}(p_0) + \left(\frac{\partial q_c}{\partial s}\right)^2 \text{var}(s) + \left(\frac{\partial q_c}{\partial p}\right)^2 \text{var}(p) \end{aligned} \quad (5)$$

So that:

$$\begin{aligned} \text{var}(q) &= \frac{1}{S_0 + P_0} + \frac{1}{S + P} \\ \text{var}(q_c) &= \frac{\left(\frac{1}{g+1}\right)^2 S_0 + P_0}{P_0^2} + \frac{\left(\frac{1}{g+1}\right)^2 S + P}{P^2} \quad (6) \end{aligned}$$

For conditions when the primary signal without phantom p_0 is much bigger than the primary signal with phantom p , the above equation can be simplified as:

$$\begin{aligned} \text{var}(q) &\approx \frac{1}{S + P} \\ \text{var}(q_c) &\approx \frac{\left(\frac{1}{g+1}\right)^2 S + P}{P^2} \quad (7) \end{aligned}$$

Therefore, the ratio of the noise of q_c and q is

$$\frac{\text{var}(q_c)}{\text{var}(q)} \approx \left[\left(\frac{1}{g+1}\right)^2 \frac{S}{P} + 1 \right] \left[\frac{S}{P} + 1 \right] \quad (8)$$

Equation (8) shows the noise is increased with the scatter reduction and correction method. The ratio will be increased with higher scatter-to-primary ratio (SPR) or lower grid blocking ratio (less photon blocked by grid). As an example, the increase of noise was calculated based on a projection image acquired using the 20 cm phantom and 1:1 grid:

$$g = 1, P = 123.1, P_0 = 10610, \frac{1}{2}S = 91.91, \frac{1}{2}S_0 = 1045$$

The ratio of the noise of q_c and q will be 3.4, which means the noise is magnified after scatter correction process. This increase of noise can outweigh the enhancement of contrast leading to degradation of CNR'.

4.1.1 Cross Scatter

As shown in Figure 3-1 and Figure 3-2, more severe artifact was observed in CBCT images acquired with a simultaneous acquisition mode (dual source scan) than those acquired with a sequential mode (single source scan) because of cross scatter between two x-ray sources. Furthermore, as shown in Tables 3-2 and 3-3, CNR' decreased in the images acquired with a simultaneous acquisition mode. Using our method, the CNR's of different acquisition modes were increased after scatter reduction and correction and were almost the same for three acquisition modes, which implied that our method improved the image quality of dual-source CBCT efficiently by removing the scatter.

In addition, the image quality and CNR' of interleaved and sequential modes were nearly the same, which demonstrates that the interleaved mode is a simple and efficient method to achieve the same image quality as the conventional single-source CBCT system at the cost of longer scanning time [25].

4.1.2 Scatter vs. Phantom Size

The amount of scatter radiation is highly dependent on the size of the object being imaged. As shown in table 3-4, CNR' dropped quickly as the phantom size

increased. As a result, scatter artifact was more severe in the larger phantom, as shown in Figure 3-3. The image quality improvement was limited in the 30cm phantom because increased scatter radiation (higher SPR) led to higher noise after scatter correction, as shown in Equation (8). As for a small phantom, such as the 15cm phantom case, the scatter artifact and degradation of CNR' were not severe; the enhancement of CNR' might be limited, as shown in Table 4-1.

Table 4-1. Comparison of the improvement of CNR' for various phantom sizes.

ROI	Phantom Size: Diameter (cm)	CNR' (15, 20 and 30cm phantom, simultaneous mode, 1:1 grid)		Improvement
		Original Data	Scatter Reduction and Correction	
1	15	73.9	182.6	147%
	20	53.4	66.9	25%
	30	12.1	14.5	20%
2	15	20.3	20.6	1%
	20	8.8	9.1	3%
	30	1.1	1.7	55%
6	15	95.6	99.8	4%
	20	48.5	57.5	19%
	30	8.2	10.4	27%
7	15	32.2	32.3	0%
	20	14.4	18.1	26%
	30	2.99	2.96	-1%

4.1.3 Grid Effect

As shown in Figure 3-4 and Table 3-5, the higher grid blocking ratio (more blocked area) will reduce scatter photons, leading to better scatter artifact reduction and CNR' enhancement. The CNR' enhancement of 4 ROIs as seen in Table 4-2 is calculated based on the data in Table 3-5.

As shown in Table 4-2, a 2:1 grid showed greater CNR' enhancement as comparing to a 1:1 grid for all inserts. This is because the grids with high grid blocking ratios blocked out more primary beams and divided each cone beam into multiple quasi-fan beams, which substantially reduced the scatters to enhance CNR'. However, higher grid blocking ratio requires more complex imaging procedures and increased number of exposures to obtain entire object information. Thus, higher grid blocking ratio may be used for imaging larger patients with severe scatter effect [27].

Table 4-2. Comparison of the improvement of CNR' enhancement for different grid blocking ratios.

CNR' Enhancement (20 cm phantom, simultaneous mode, 1:1 and 2:1 grid)			
ROI	Grid Blocking Ratio	Scatter Reduction Only	Scatter Reduction and Correction
1	1:1	19%	25%
	2:1	63%	102%
2	1:1	15%	3%
	2:1	27%	18%
6	1:1	3%	19%
	2:1	71%	76%
7	1:1	28%	26%
	2:1	47%	43%

4.2 Reconstruction Algorithm

Figure 3-5 showed that the images reconstructed by iterative reconstruction method with total variation (TV) were smoother than the images reconstructed by FDK. In addition, as shown in Table 3-6, CNR's for most inserts were improved by TV reconstruction algorithm due to the noise-suppression by the TV algorithm. This

improvement is especially dramatic for the scatter reduced and corrected images, where noise has been elevated due to the scatter correction process.

4.3 Limitation of Scatter Correction with Pre-patient Grid

Although the scatter reduction and correction with a pre-patient grid showed effective scatter artifact removal and enhancement of CNR' and HU number linearity, there are some limitations of our method: noise, image lag and artifact cause by imperfect grid movement during acquisition. Noise may be reduced by using noise-suppression reconstruction method such as iterative method used in our project. The other two limitations were mainly caused by our manual move of the grid after each scan, which can be solved by synchronized-moving-grid (SMOG) system. In the SMOG system, as described in [27], the grid is controlled accurately by a motor to move back and forth at each scan angle to acquire all complementary projections before moving to the next scan angle.

4.3.1 Noise

As shown in Equation (8), the noise may increase by a factor of 3.4 after scatter correction, which may cause the reduction of CNR'. Some noise suppression methods such as iterative reconstruction method and noise suppression post-processing methods may be used to improve CNR'.

4.3.2 Image Lag

Image lag was seen during the interleaved acquisition mode (the two tubes are interleaved firing) in our experiments. As shown in Figure 4-1, the image lag was evident in the image acquired when the corresponding tube was not firing. This image lag can cause skin line artifact in CBCT, and can be removed by using the SMOG system [27].

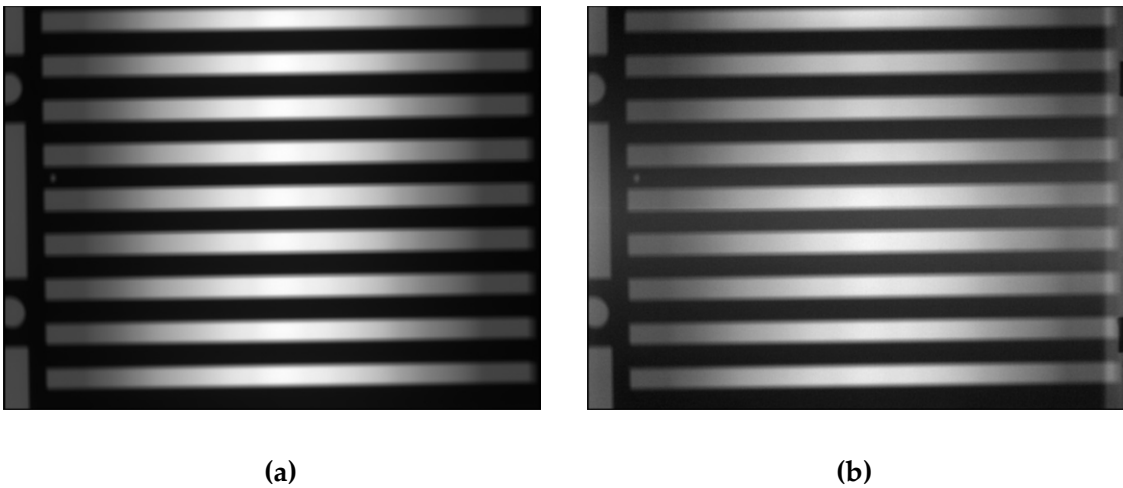


Figure 4-1. An example of image Lag. (a): exposure image acquired in an empty scan (pixel value min: 0, max: 14545). (b): image acquired by the same detector when the corresponding tube was not firing (pixel value min: 0, max: 283).

4.3.3 Artifact of Grid Misalignment

As grids were moved manually in our study, there were gaps (about one or two lines) in the merged projection caused by misalignment of the grid, as shown in Figure 4-2. This can cause streak artifacts in the reconstructed image after scatter correction, especially in the slice corresponding to the gaps in the projections, as shown in Figure 4-3.

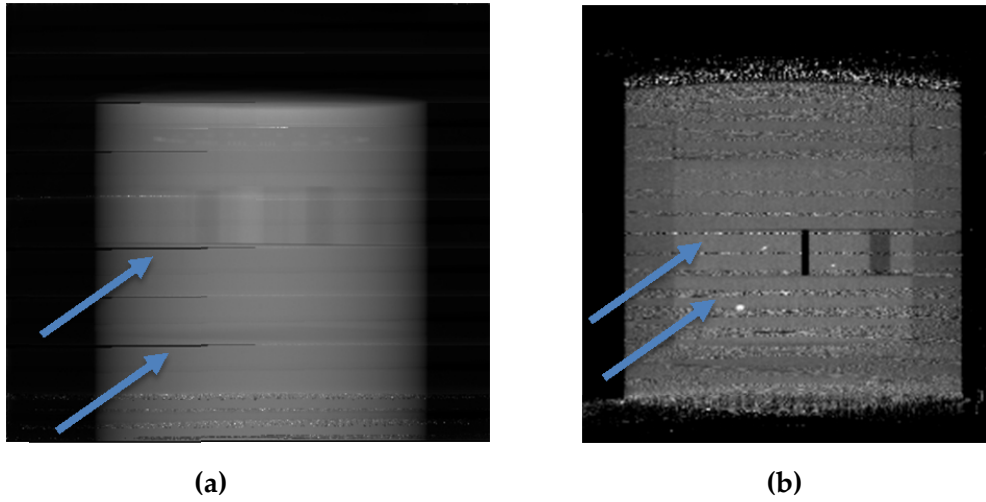


Figure 4-2. An example of grid misalignment. (a). One merged projection for a CATphan of 20cm diameter acquired with a simultaneous mode using 1:1 grid. The arrows point out gaps caused by the misalignment between the grid shifts. (b). a sagittal slice of the reconstructed CBCT image. The noise region as pointed by arrows is caused by the gap in the projections in (a).

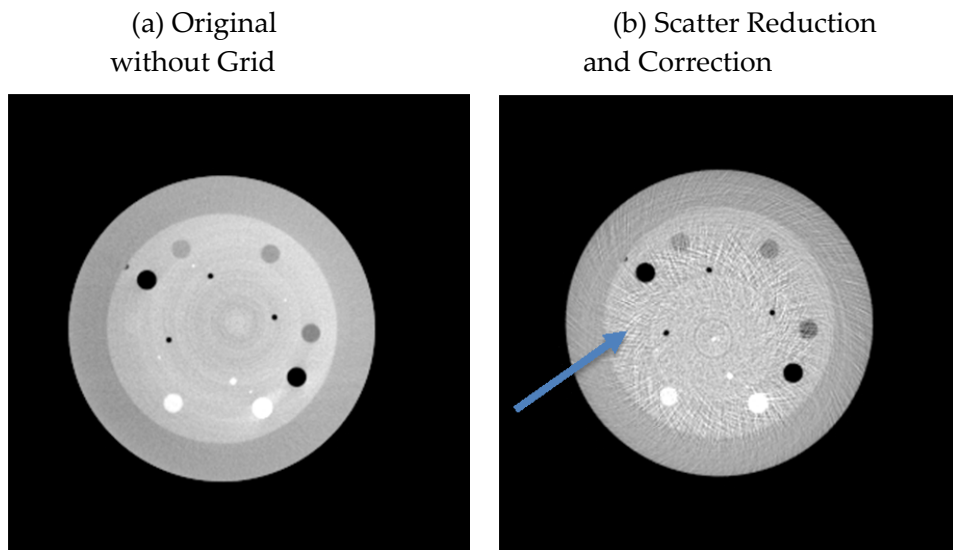


Figure 4-3. Reconstructed axial images of a CATphan of 20cm diameter scanned by the simultaneous acquisition mode. 1:1 grid was applied for scatter reduction and scatter correction. (a) without grid and (b) scatter reduction and scatter correction. Image is displayed with a window width of 1000HU and a window level of -200HU. As the arrows shown, streak artifacts caused by grid misalignment are shown as the noise region in the reconstructed image.

In this case, CNR's of 8 inserts of different slices in the CTP 404 module were drawn in Figure 4-4 and Figure 4-5.

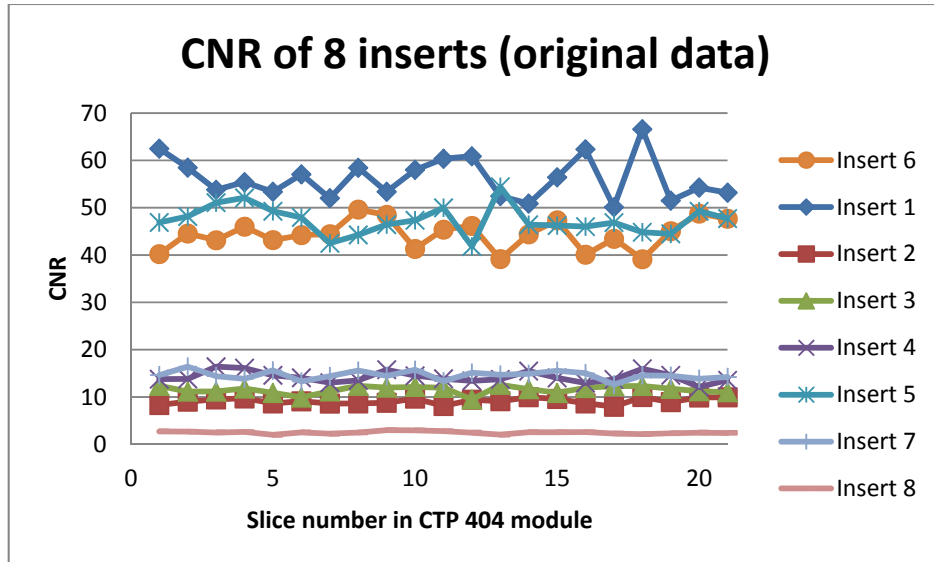


Figure 4-4. CNR' of 8 inserts in different reconstructed axial slices without grid using 20 cm CATphan acquired by simultaneous mode.

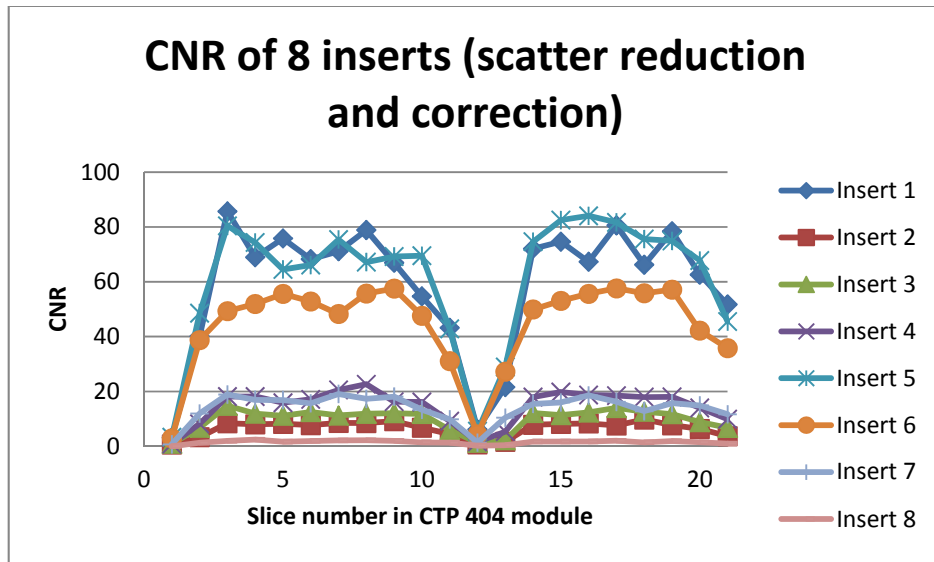


Figure 4-5. CNR' of 8 inserts in different reconstructed axial slices after scatter correction with 1:1 grid using 20 cm CATphan acquired by simultaneous mode.

From the above figures, the CNR's of 8 inserts drop quickly to nearly 0 in the same slice. This artifact can be solved by using SMOG system, in which the grid was more accurately positioned by a motor at complementary positions without any gaps. Increasing the unblock area slightly can also avoid this problem by acquiring more overlapping data.

5. Conclusion

A method using pre-patient moving grid has been developed for effective reduction of scatter artifacts for a dual-source CBCT system. Experimental result showed that scatter reduction alone reduced the scatter artifacts and enhanced the CNR' of the CBCT images. Addition of the scatter correction process removed the almost completely scatter artifacts with a cost of degrading the CNR' due to the noise increase by the scatter subtraction and negative log transformation. The HU linearity was slightly improved to nearly 0.9999 by the scatter reduction and correction method.

The enhancement of CNR' is weakly correlated to the phantom size. Grids with higher blocking ratio (more blocked area) achieved better CNR' and artifact reduction with the drawbacks of more complex procedure and increased number of exposures. Scatter artifact is the most severe in the dual-source simultaneous scan mode and is less severe in the interleaved acquisition mode. Iterative reconstruction with TV regularization can effectively reduce the noise introduced by scatter correction to enhance the CNR'.

In summary, our method with a pre-patient grid can effectively reduce the scatter artifacts and enhance CNR' and CT number linearity for the dual-source CBCT system. The settings such as grid blocking ratio and acquisition mode can further be optimized based on the specific patient condition to achieve better image quality.

References

1. Bushberg JT, Boone JM: **The essential physics of medical imaging**: Lippincott Williams & Wilkins; 2011.
2. Johnson TR, Krauss B, Sedlmair M, Grasruck M, Bruder H, Morhard D, Fink C, Weckbach S, Lenhard M, Schmidt B: **Material differentiation by dual energy CT: initial experience**. *European radiology* 2007, **17**(6):1510-1517.
3. Kyriakou Y, Kalender WA: **X-ray scatter data for flat-panel detector CT**. *Physica Medica* 2007, **23**(1):3-15.
4. Siewerdsen JH, Jaffray DA: **Cone-beam computed tomography with a flat-panel imager: magnitude and effects of x-ray scatter**. *Medical physics* 2001, **28**(2):220-231.
5. McAdams HP, Ravin CE: **Comparative scatter and dose performance of slot-scan and full-field digital chest radiography systems**. *Radiology* 2005, **235**:940-949.
6. Neitzel U: **Grids or air gaps for scatter reduction in digital radiography: a model calculation**. *Medical physics* 1992, **19**(2):475-481.
7. Sorenson JA, Niklason LT, Knutti DF: **Performance characteristics of improved antiscatter grids**. *Medical physics* 1980, **7**(5):525-528.
8. Wiegert J, Bertram M, Schaefer D, Conrads N, Timmer J, Aach T, Rose G: **Performance of standard fluoroscopy anti-scatter grids in flat detector based cone beam CT**. In: *Proc SPIE: 2004*; 2004: 67-78.
9. Zhu L, Xie Y, Wang J, Xing L: **Scatter correction for cone-beam CT in radiation therapy**. *Medical physics* 2009, **36**:2258-2268.
10. Rührnschopf E-P, Klingenbeck K: **A general framework and review of scatter correction methods in x-ray cone-beam computerized tomography. Part 1: Scatter compensation approaches**. *Medical physics* 2011, **38**(7):4296-4311.
11. Floyd Jr CE, Baker JA, LO JY, RAVIN CE: **Posterior beam-stop method for scatter fraction measurement in digital radiography**. *Investigative radiology* 1992, **27**(2):119-123.

12. Floyd CE, Beatty PT, Ravin CE: **Scatter compensation in digital chest radiography using Fourier deconvolution.** *Investigative radiology* 1989, **24**(1):30-33.
13. Hinshaw DA, Dobbins III JT: **Plate scatter correction for improved performance in dual - energy imaging.** *Medical physics* 1996, **23**(6):871-876.
14. Akbarzadeh A, Ay M, Ghadiri H, Sarkar S, Zaidi H: **Measurement of scattered radiation in a volumetric 64-slice CT scanner using three experimental techniques.** *Physics in medicine and biology* 2010, **55**(8):2269.
15. Ning R, Tang X, Conover DL: **X-ray scatter suppression algorithm for cone-beam volume CT.** In: *Medical Imaging 2002: 2002: International Society for Optics and Photonics*; 2002: 774-781.
16. Ning R, Tang X, Conover D: **X-ray scatter correction algorithm for cone beam CT imaging.** *Medical physics* 2004, **31**(5):1195-1202.
17. Jin J-Y, Ren L, Liu Q, Kim J, Wen N, Guan H, Movsas B, Chetty IJ: **Combining scatter reduction and correction to improve image quality in cone-beam computed tomography (CBCT).** *Medical physics* 2010, **37**(11):5634-5644.
18. Zhu L, Strobel N, Fahrig R: **X-ray scatter correction for cone-beam CT using moving blocker array.** In: *Medical imaging: 2005: International Society for Optics and Photonics*; 2005: 251-258.
19. Zhu L, Bennett NR, Fahrig R: **Scatter correction method for X-ray CT using primary modulation: Theory and preliminary results.** *Medical Imaging, IEEE Transactions on* 2006, **25**(12):1573-1587.
20. Zhu L, StarLack J, Bennett NR, Li T, Xing L, Fahrig R: **Improved scatter correction for x-ray conebeam CT using primary modulation.** In: *Medical Imaging: 2007: International Society for Optics and Photonics*; 2007: 65101U-65101U-65108.
21. Gao H, Zhu L, Fahrig R: **Optimization of system parameters for modulator design in x-ray scatter correction using primary modulation.** In: *SPIE Medical Imaging: 2010: International Society for Optics and Photonics*; 2010: 76222A-76222A-76229.
22. Zhu L, Wang J, Xing L: **Noise suppression in scatter correction for cone-beam CT.** *Medical physics* 2009, **36**(3):741-752.

23. Jin J-Y, Ren L, Liu Q, Kim J, Wen N, Guan H, Movsas B, Chetty IJ: **Combining scatter reduction and correction to improve image quality in cone-beam computed tomography (CBCT)**. *Medical physics* 2010, **37**:5634-5644.
24. Ren L, Yin F-F, Chetty IJ, Jaffray DA, Jin J-Y: **Feasibility study of a synchronized-moving-grid (SMOG) system to improve image quality in cone-beam computed tomography (CBCT)**. *Medical physics* 2012, **39**:5099-5110.
25. Giles W, Bowsher J, Li H, Yin F-F: **Interleaved acquisition for cross scatter avoidance in dual cone-beam CT**. *Medical physics* 2012, **39**(12):7719-7728.
26. Mail N, Moseley D, Siewerdsen J, Jaffray D: **The influence of bowtie filtration on cone-beam CT image quality**. *Medical physics* 2008, **36**(1):22-32.
27. Ren L, Yin F-F, Chetty IJ, Jaffray DA, Jin J-Y: **Feasibility study of a synchronized-moving-grid (SMOG) system to improve image quality in cone-beam computed tomography (CBCT)**. *Medical physics* 2012, **39**(8):5099-5110.
28. Feldkamp L, Davis L, Kress J: **Practical cone-beam algorithm**. *JOSA A* 1984, **1**(6):612-619.
29. Erdogan H, Fessler JA: **Ordered subsets algorithms for transmission tomography**. *Physics in medicine and biology* 1999, **44**(11):2835.
30. Sidky EY, Pan X: **Image reconstruction in circular cone-beam computed tomography by constrained, total-variation minimization**. *Physics in medicine and biology* 2008, **53**(17):4777.
31. Sidky EY, Duchin Y, Pan X, Ullberg C: **A constrained, total-variation minimization algorithm for low-intensity x-ray CT**. *Medical physics* 2011, **38**(S1):S117-S125.
32. Kanamori H, Nakamori N, Inoue K, Takenaka E: **Effects of scattered X-rays on CT images**. *Physics in medicine and biology* 1985, **30**(3):239.